Science Advances
AAAS

Supplementary Materials for

A solid-to-solid metallic conversion electrochemistry toward 91% zinc utilization for sustainable aqueous batteries

Zhiguo Hou *et al.*

Corresponding author: Dongliang Chao, chaod@fudan.edu.cn

Sci. Adv. **8**, eabp8960 (2022)
DOI: 10.1126/sciadv.abp8960

This PDF file includes:

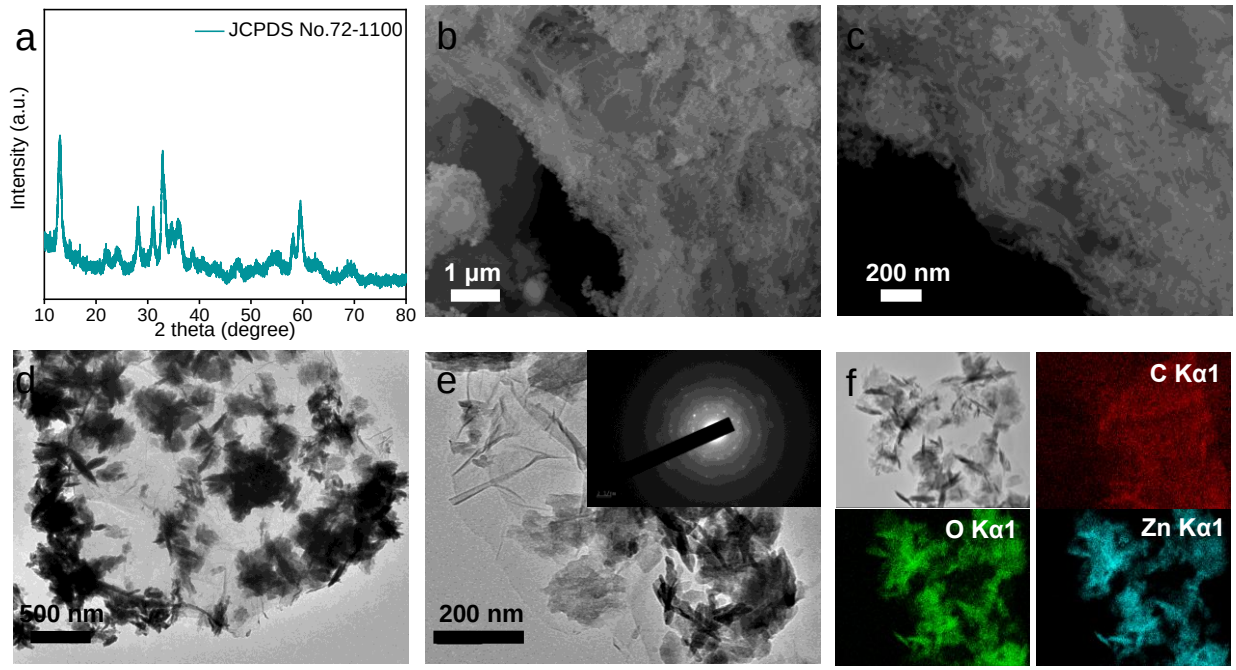

Fig. S1. Characterization of the as-prepared ZZG composite. (a) XRD pattern of as-prepared ZZG composite. (b) and (c) SEM images of ZZG composite. (d) TEM image of ZZG composite. (e) TEM image and SAED (insertion) pattern of ZZG composite. (e) EDS mapping images of ZZG composite.

Supplementary Note S1: **Analysis of structure and morphology of ZZG.** The XRD reveals the high purity of the formed monoclinic phase (JCPDS No. 72-1100). Moreover, confirmatory evidence is provided by the X-ray photoelectron spectroscopy (XPS) results in Fig. S1. The Scanning electron microscope (SEM, **S1**b and **S1**c) images show that the ZZG composite displays agglomerated nanoparticles coated on graphene sheets. The transmission electron microscope (TEM) image (**S1**d and **S1**e) further reveals that the ZZG nanoparticles exhibit uniform morphology of nanoplates with a diameter ranging from 50 to 100 nm, which are uniformly and firmly composited with the graphene sheet. The polycrystalline character of ZZG nanoplates is verified by the selected area electron diffraction (SAED) pattern (insertion in **S1**e). The TEM/energy-dispersive X-ray spectroscopy (EDS) mapping images (**S1**f) of ZZG composite show the homogeneous distribution of Zn, C, and O.

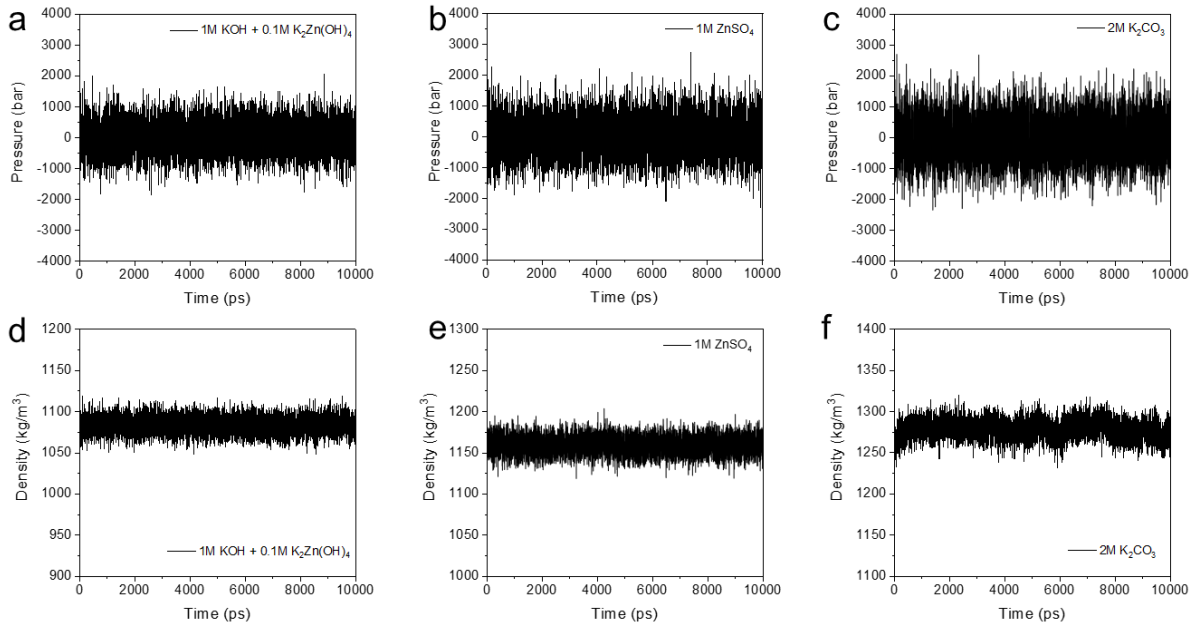

Fig. S2. **Pressure and density during the simulation time for different electrolytes.** (a) 1M KOH and 0.1M $K_2Zn(OH)_4$, (b) 2M $ZnSO_4$, (c) 2M K_2CO_3; density during the simulation time for (d) 1M KOH and 0.1M $K_2Zn(OH)_4$, (e) 2M $ZnSO_4$, (f) 2M K_2CO_3.

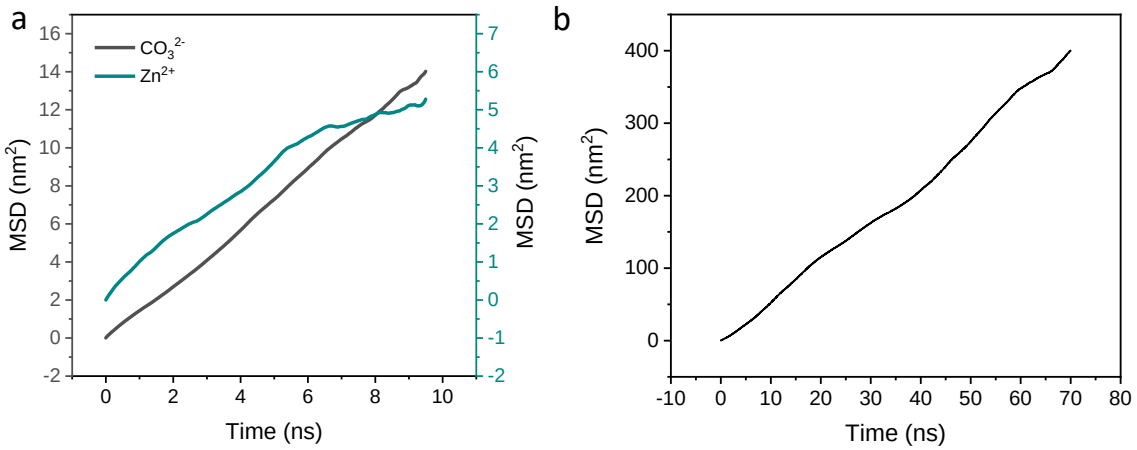

Fig. S3. Mean square displacement as a function of time for different ions. (a) Mean square displacement (MSD) as a function of time for CO_3^{2-} and Zn^{2+}. (b) MSD as a function of time for OH^-.

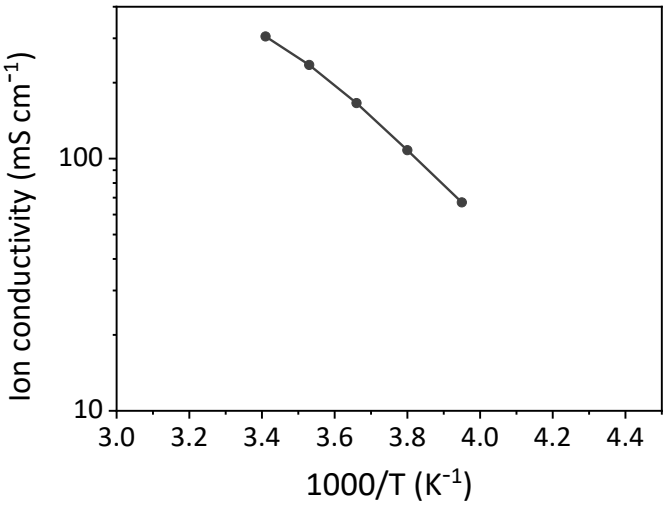

Fig. S4. The Arrhenius plots of the ion conductivity for 2 M K_2CO_3 electrolyte.

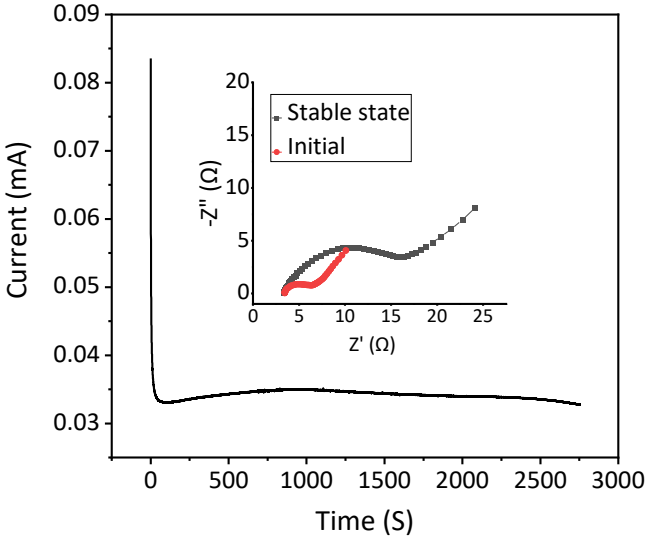

Fig. S5. Polarization curve and Nyquist plot. Polarization curves obtained by chronoamperometry for the ZZG+Zn || 2M K_2CO_3 || ZZG+Zn symmetrical cell at 25 °C. (Inset) Nyquist plots of the symmetrical cell.

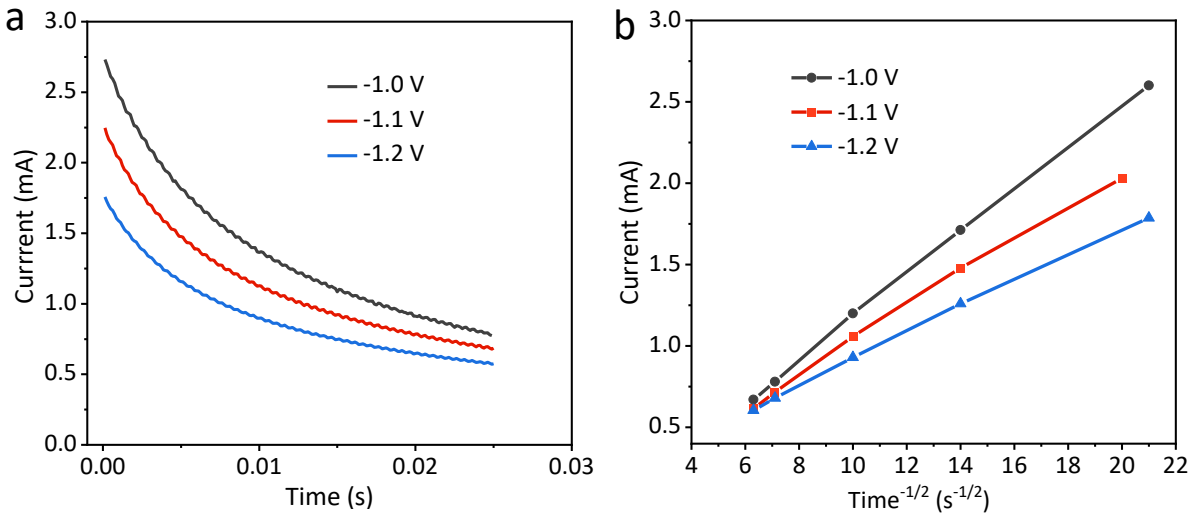

Fig. S6. The potentiostatic analysis of the diffusion current *i vs.* $t^{-1/2}$ for Zn plates. (a) Potentiostatic measurements of *i vs. t* at –1.2, –1.1 and –1.0 V for Zn plates. (b) *i vs.* $t^{-1/2}$ from potentiostatic measurements at –1.2, –1.1 and –1.0 V for Zn plates. Potentials are measured vs. HgO/Hg reference electrode and converted to SHE for convenient comparison.

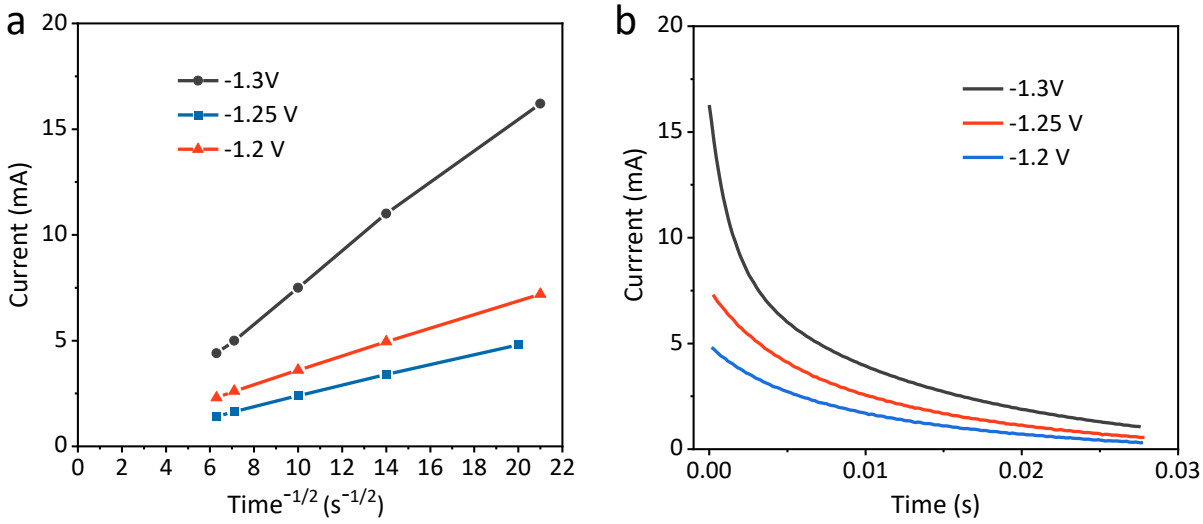

Fig. S7. The potentiostatic analysis of *i vs.* $t^{-1/2}$ for ZZG electrodes. (a) Potentiostatic measurements of *i vs. t* at –1.3, –1.25 and –1.2 V for ZZG electrodes. (b) *i vs.* $t^{-1/2}$ from potentiostatic measurements at –1.3, –1.25 and –1.2 V for ZZG electrodes.

Supplementary Note S2: **Potentiostatic measurement of the diffusion current *i vs.* $t^{-1/2}$.** The plot of potentiostat measurements of *i vs.* $t^{-1/2}$ shows that the reduction of ZZG is completely diffusion-controlled at all potentials :

$i = n FAC_s^o (D/\pi t)^{1/2}$

$= 2FAC_{CO3}^{2-}(D_{CO3}^{2-}/\pi t)^{1/2} + 2FAC_{Zn}^{2+} (D_{Zn}^{2+}/\pi t)^{1/2} + FAC_{OH-}(D_{OH-}/\pi t)^{1/2}$

The C_{CO3}^{2-} is the surface concentration of a CO_3^{2-} species equilibrium with the ZZG dissolution. A is area of electrode (1 cm^2), F is Faraday constant, D is the diffusion coefficient of species, i.e., D_{Zn}^{2+} (0.89×10^{-6} cm^2 s^{-1}), D_{CO3}^{2-} (2.540×10^{-6} cm^2 s^{-1}) and, D_{OH-} (3.8×10^{-6} cm^2 s^{-1}).

The solubility of basic zinc carbonate is 0.042 g L^{-1} (8.0×10^{-5} M). So, the C_{CO3}^{2-} is 1.6×10^{-4} M, the C_{Zn}^{2+} is 4.0×10^{-4} M and the C_{OH-} is 4.8×10^{-4} M. The *i* is about 16.2 mA at 2 ms under −1.3 V *vs.* SHE, which is about the sum of $2FAC_{CO3}^{2-}(D_{CO3}^{2-}/\pi t)^{1/2}$ and $FAC_{OH-}(D_{OH-}/\pi t)^{1/2}$, much lower than the calculated current according to the above equation. It is suggested that the current is mostly ascribed to the diffusion of CO_3^{2-} and OH^-. The diffusion of Zn^{2+} from the electrode to the electrolyte is very limited, which is consistent with the results of the faster diffusion coefficient of CO_3^{2-} and OH^-.

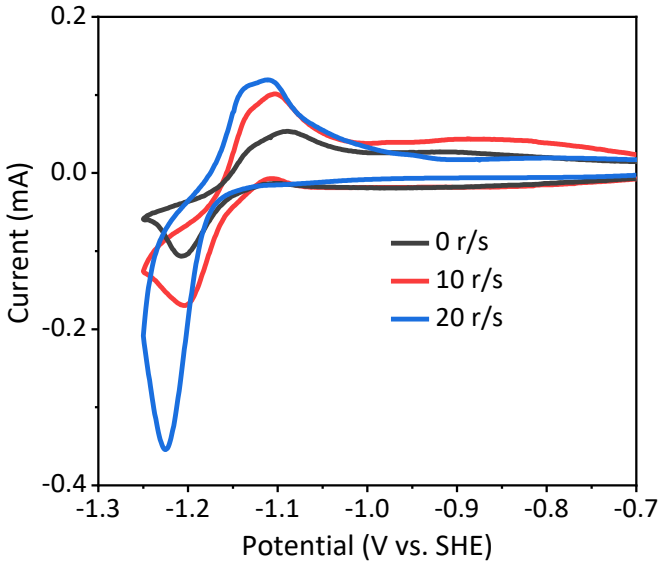

Fig. S8. CVs of an electrogalvanizing rotating disc electrode. It is recorded on the polarization of an electrogalvanizing rotating disc electrode (surface areas 0.5 cm^{-2}) in de-oxygenated 2 M K_2CO_3 solution at a scan rate of 1 mV s^{-1}. The rotation speeds are 0, 10, and 20 rps.

Supplementary Note S3: **Discussion for the rotating disk electrode test.** Fig. S8 shows that the CV curves of basic zinc carbonate electrode mark rotation speed dependence both at cathodic and anodic peaks. It is suggested that the reduction of Zn^{2+} and oxidation of Zn are both diffusion-limited processes. As the rotation speed increases, the cathodic peak current also increases, which is contrary to the results of lead-acid batteries (*G. Archdale, J.A. Harrison, J. Electroanal. Chem. 34 (1972) 21.*). For the lead-acid battery, when the electrode is rotated during the anodic polarization, the current increases rapidly, as there are no Pb^{2+} ions to be reduced due to the rotation of the electrode. The faster diffusion of CO_3^{2-} than Zn^{2+} is theoretically calculated. Here, it is verified that if the diffusion of Zn^{2+} is faster than CO_3^{2-}, the reduction peak of Zn^{2+} should be decreased with rotation speed increased. As the reaction continues, the Zn^{2+} will be thrown out into the bulk of the solution as a result of the rotation of the electrode.

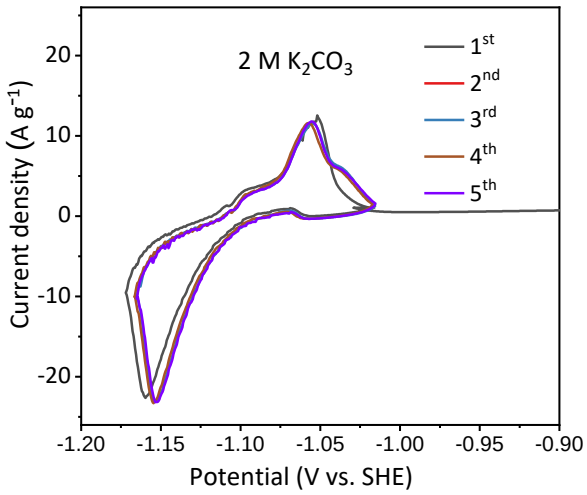

Fig. S9. CV curves of ZZG anode in 2 M K_2CO_3 electrolyte. The scan rate is 0.5 mV s^{-1} between −1.0 V and −1.2 V *vs.* SHE.

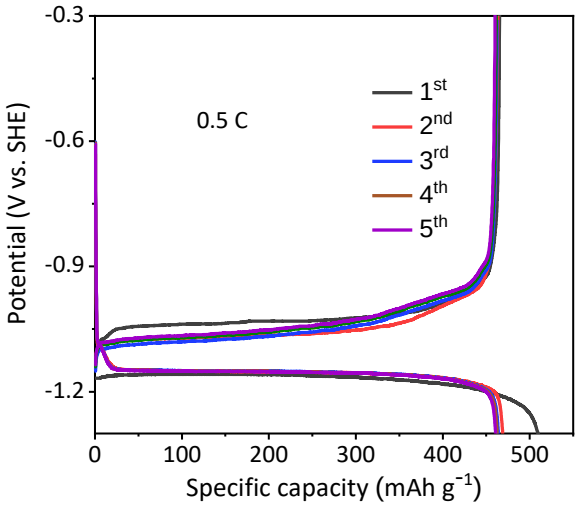

Fig. S10. Charge/discharge curves of ZZG anode in 2 M K_2CO_3 electrolyte. The charging/discharging rate is 0.5 C between −0.3 V and −1.3 V *vs.* SHE.

Supplementary Note S4: **Calculation of utilization of Zn.** The zinc utilization is a crucial index for a practical battery. Commonly, most previous works adopted impractical full-cell components using a large zinc excess to prevent premature depletion of zinc[3].

The zinc utilization of $2ZnCO_3{\cdot}3Zn(OH)_2$ in the asymmetric cell of anode is calculated as 95.7% based on the reversible capacity of $2ZnCO_3 \cdot 3Zn(OH)_2$ in the ZZG electrode. The theoretical specific capacity of $2ZnCO_3{\cdot}3Zn(OH)_2$ is about 488.3 (96500×10/(3.6×548.9)) mAh g^{-1}. The reversible capacity of ZZG in the asymmetric cell is about 458 mAh g^{-1}. So the zinc utilization of $2ZnCO_3{\cdot}3Zn(OH)_2$ is about 95.7% (458/0.98/488.3) in the asymmetric cell.

The zinc utilization of $2ZnCO_3 \cdot 3Zn(OH)_2$ in the full cell is calculated as 91.3%. The theoretical specific capacity of $2ZnCO_3{\cdot}3Zn(OH)_2$ is about 488.3 (96500×10/(3.6×548.9)) mAh g^{-1}. The reversible capacity of ZZG in Ni-ZZG battery is about 243 mAh g^{-1} based on Ni-based cathode (437 mAh g^{-1} based on ZZG electrode). So the zinc utilization of $2ZnCO_3{\cdot}3Zn(OH)_2$ in the Ni-ZZG full cell is 91.3% (437/0.98/488.3).

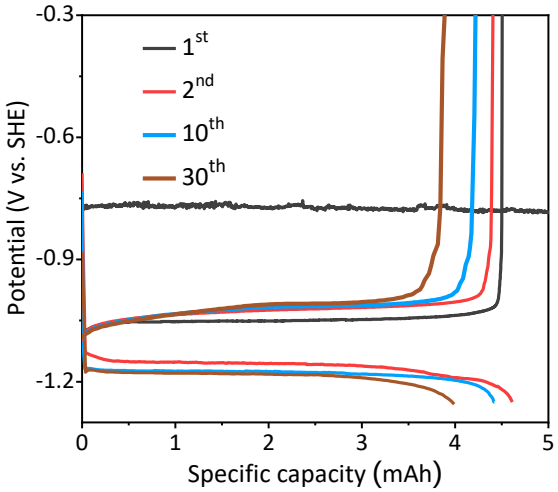

Fig. S11. Galvanostatic discharge/charge curves of Zn metal anode in 2 M K_2CO_3 electrolyte. The metallic Zn electrode was prepared by Zn deposition on carbon paper in a 1 M $ZnSO_4$ electrolyte with area capacity of 5 mAh. The operation is carried out in the glove box to prevent the oxidation of electro-deposition Zn. The electrochemical performances of electro-deposition Zn were tested in 2 M K_2CO_3 electrolyte using three-electrode testing system, in which a piece of Zn metal sheet and an HgO/Hg electrode (0.095 V *vs.* SHE) served as counter and reference electrodes, respectively.

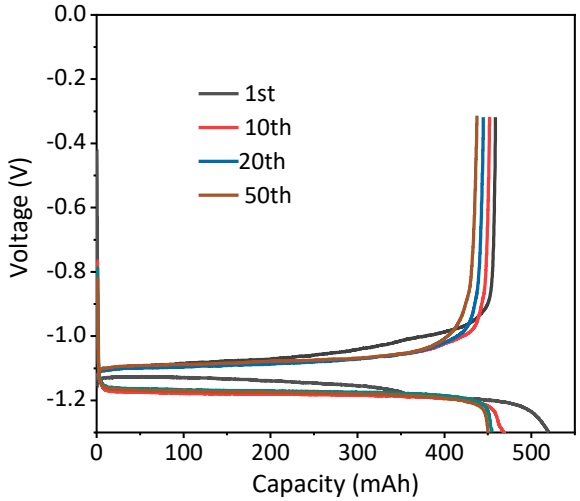

Fig. S12. Charge/discharge curves of ZZG anode in 2 M K_2CO_3 electrolyte with Pt as counter electrode. Three-electrode testing system is used at a rate of 0.5 C between −0.3 V and −1.3 V *vs.* SHE, where Pt electrode and HgO/Hg electrode served as counter and reference electrodes, respectively.

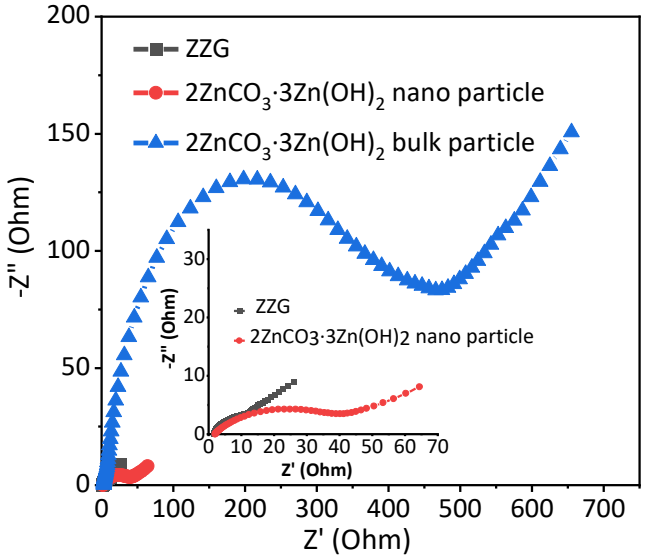

Fig. S13. Nyquist plots for ZZG, $2ZnCO_3·3Zn(OH)_2$ bulk particles and $2ZnCO_3·3Zn(OH)_2$ nanoparticles. The EIS tests were carried out from 0.01 Hz to 100k Hz in a three electrode system in which the ZZG, $2ZnCO_3·3Zn(OH)_2$ bulk particle and $2ZnCO_3·3Zn(OH)_2$ nano particle were used as working electrodes, Zn metal sheet and an HgO/Hg electrode served as counter and reference electrodes, respectively.

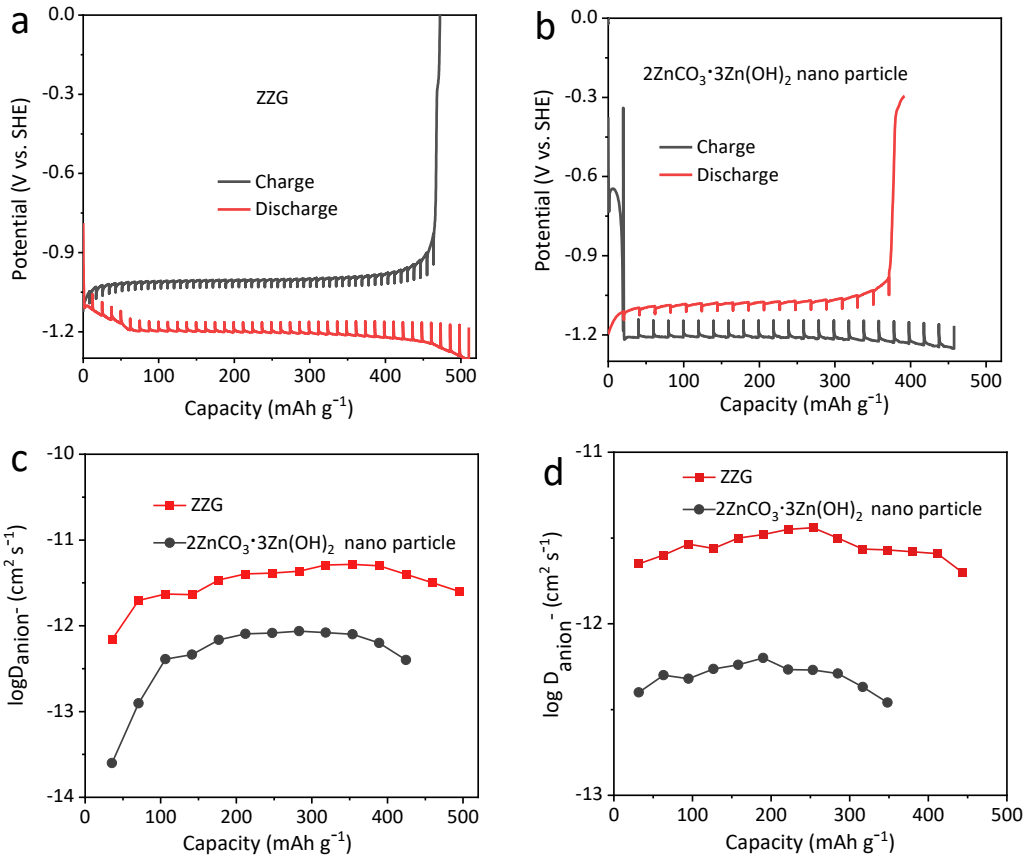

Fig. S14. Galvanostatic intermittent titration technique curves and ion diffusion coefficients. Galvanostatic intermittent titration technique curves of (a) ZZG and (b) $2ZnCO_3 \cdot 3Zn(OH)_2$ nanoparticles during initial discharge and charge process, respectively. The anions diffusion coefficient curves of ZZG and $2ZnCO_3 \cdot 3Zn(OH)_2$ nanoparticles at initial discharge (c) and charge (d) process, respectively.

The GITT results were obtained in a three-electrode system in which the ZZG and $2ZnCO_3 \cdot 3Zn(OH)_2$ nanoparticles were used as working electrodes, Zn metal sheet and an HgO/Hg electrode served as counter and reference electrodes, respectively. The charging/discharging of the electrode is achieved by applying a constant current flux (0.5 A g^{-1}) for a limited period (90 s), and then the cell is allowed to relax to its new steady-state potential (30 min) between -0.3 and -1.3 V vs. SHE. The diffusion coefficient for anion can be determined by using Fick's second law of diffusion:

$$\mathrm{D} = \frac{4}{\pi\tau}\left(\frac{m_B V_m}{M_B A}\right)^2 \left(\frac{\Delta E_s}{\Delta E_\tau}\right)^2$$

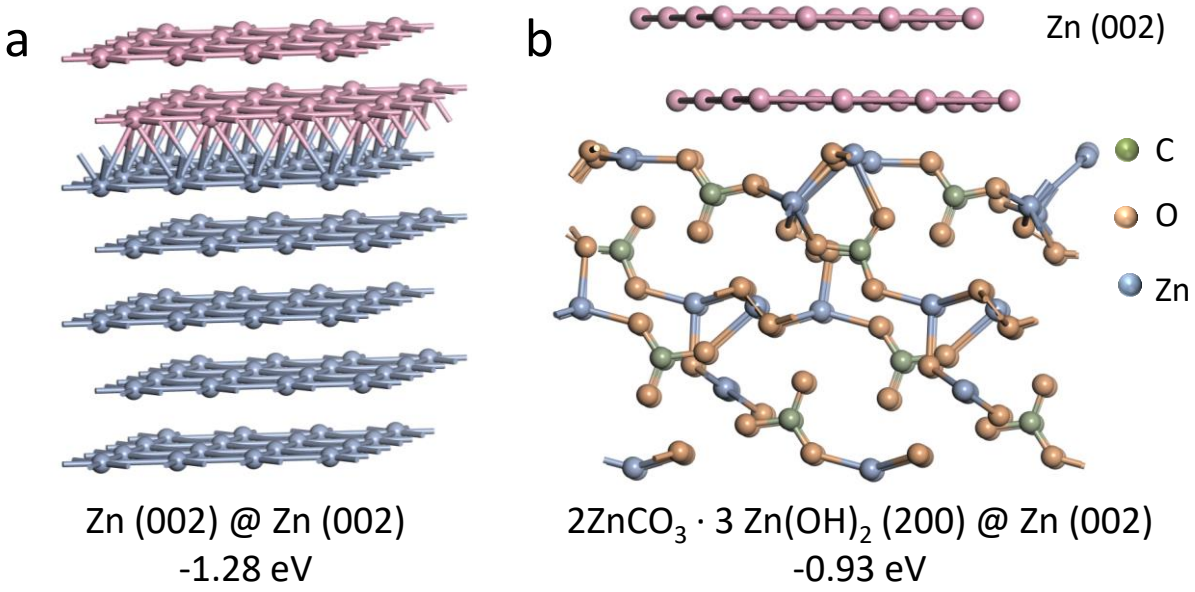

Fig. S15. Calculated binding energy. (a) Binding energy between Zn (002) face and Zn (002) face. (b) Binding energy between Zn (002) face and $2ZnCO_3 \cdot 3Zn(OH)_2$ (200) face.

The CASTEP[45] for all the DFT calculations within the generalized gradient approximation (GGA) using the Perdew-Burkee-Ernzerhof (PBE) functional formulation[46] were used in this work. A 2 × 2 × 1 supercell of Zn (002) and $2ZnCO_3 \cdot 3Zn(OH)_2$ (200) was constructed to research the model. A plane-wave basis set with a cutoff energy of 400 eV to guarantee the convergence of the total energy and the electronic minimization parameter is set as 10^{-6} eV. All structures are fully relaxed until the force on each atom is smaller than 0.01 eV/Å. Vacuum layer is added on the surfaces of Zn and $2ZnCO_3 \cdot 3Zn(OH)_2$ was 20 Å, in which a Monkhorst-Pack K-point mesh of 2 × 2 × 1 was included.

Then the binding energy E_b for all the possible configurations can be obtained by

$$E_b = E_{total} - E_{surface} - E_{zn\_layer}$$

where E_{total} , E_{sur} and $E_{Zn_}$atom stand for the total energy of the system after composite with Zn (200) layer, the energy of pristine surface and the energy of double Zn (002), respectively.

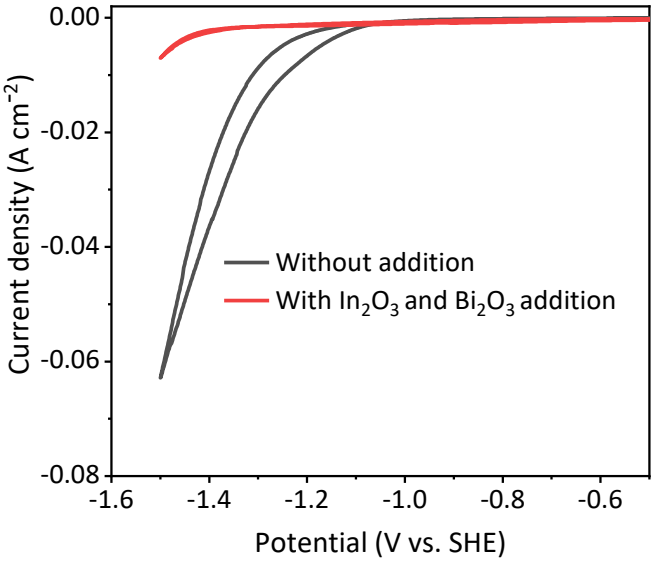

Fig. S16. CV results of electrodes in 2 M K_2CO_3 electrolyte. The electrodes are prepared with 1% In_2O_3, 1% Bi_2O_3, 90% graphite, 4% carbon black and 4% PTFE and the contrast is prepared with 92% graphite, 4% carbon black and 4% PTFE.

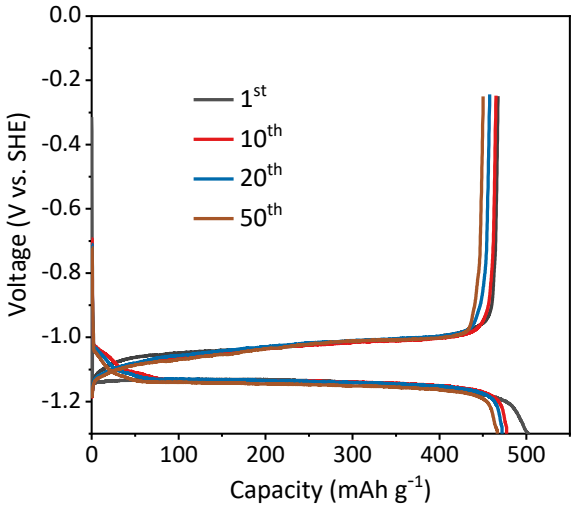

Fig. S17. Charge/discharge curves of ZZG anode with 3 wt% In_2O_3 and 3 wt% Bi_2O_3 addition. Three-electrode testing system is used in 2 M K_2CO_3 electrolyte at a rate of 0.5 C between −0.3 V and −1.3 V *vs.* SHE. The Zn metal sheet and HgO/Hg electrode serve as counter and reference electrodes, respectively. With the increasing addition of In_2O_3 (3 wt%) and Bi_2O_3 (3 wt%), the initial coulombic efficiecy can be increased to 93.3% at 0.5 C, and the average Coulombic efficiency can be increased to *ca.* 98.9% after the initial cycle.

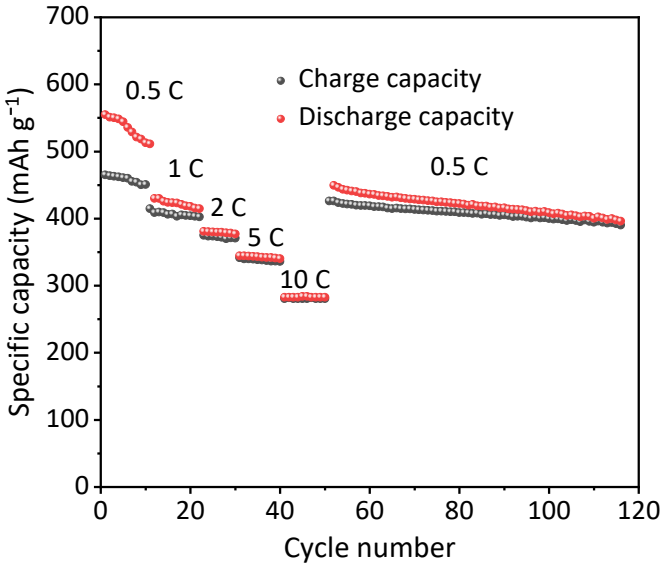

Fig. S18. ZZG cycle performance without In_2O_3 and Bi_2O_3 additions. Three-electrode testing system is used in 2 M K_2CO_3 electrolyte at a rate of 0.5 C between −0.3 V and −1.3 V *vs.* SHE. The Zn metal sheet and HgO/Hg electrode serve as counter and reference electrodes, respectively.

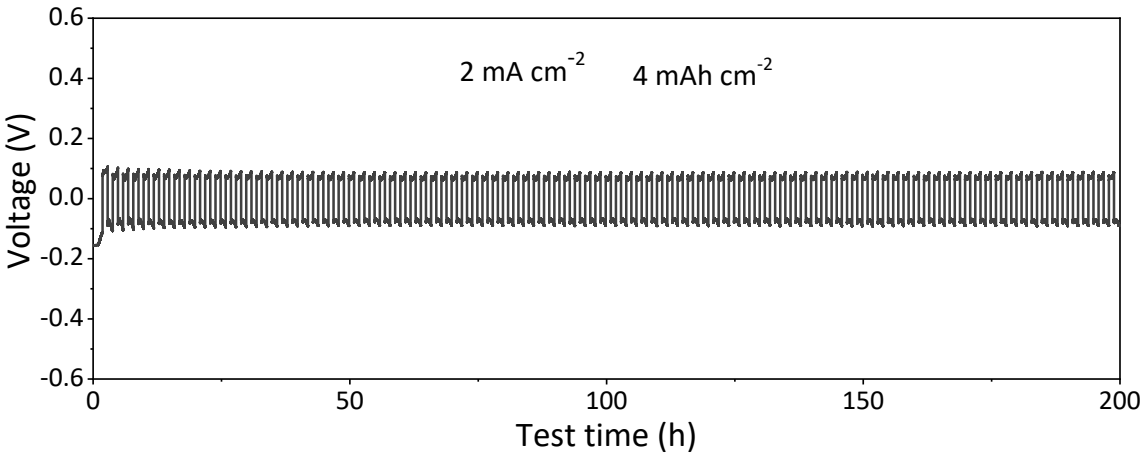

Fig. S19. Cycling performance in ZZG+Zn || ZZG+Zn symmetric cell at 2 mA cm^{-2} for 4 mAh cm^{-2}.

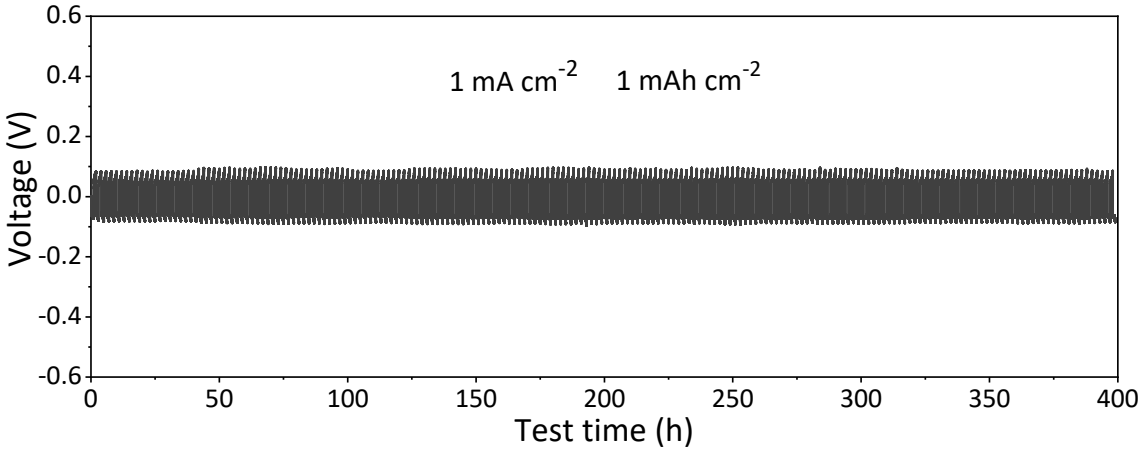

Fig. S20. Charge/discharge curves of symmetric half reduced ZZG electrode. ZZG || 2 M K_2CO_3 || ZZG with half reduced ZZG electrode cell is tested with current density of 1 mA cm^{-2} and capacity of 1 mAh cm^{-2}.

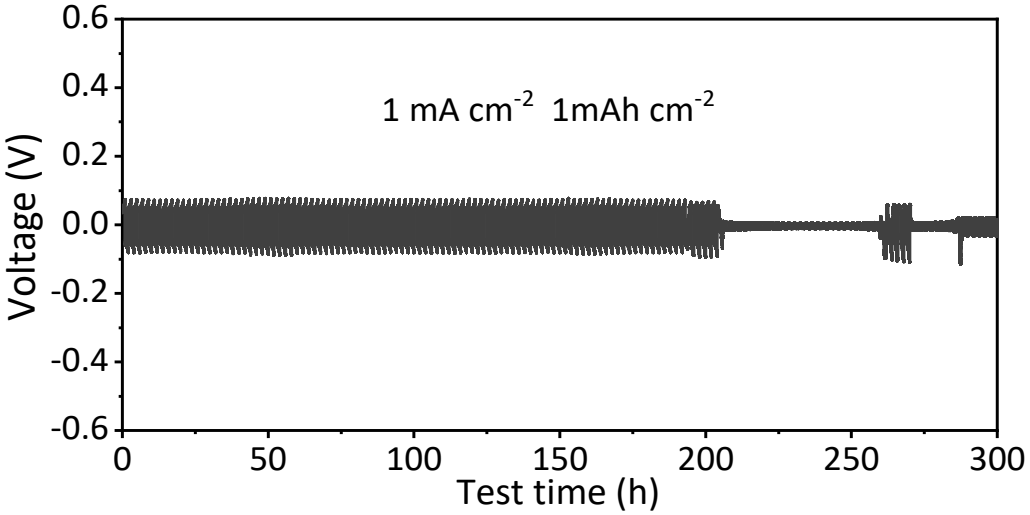

Fig. S21. Charge/discharge curves of symmetric ZZG+Zn cell in 6 M KOH + saturated ZnO electrolyte. ZZG+Zn || 6 M KOH + saturated ZnO || ZZG+Zn cell is tested with a current density of 1 mA cm^{-2} and capacity of 1 mAh cm^{-2}.

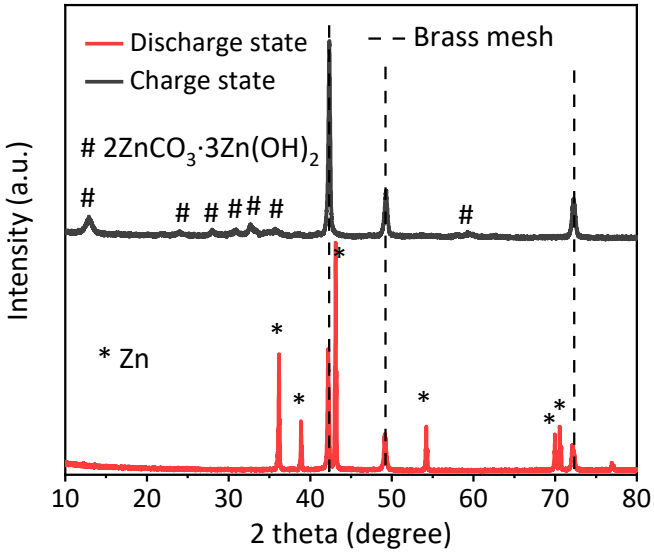

Fig. S22. XRD patterns of ZZG composite anode at the 5th discharge and charge state, respectively.

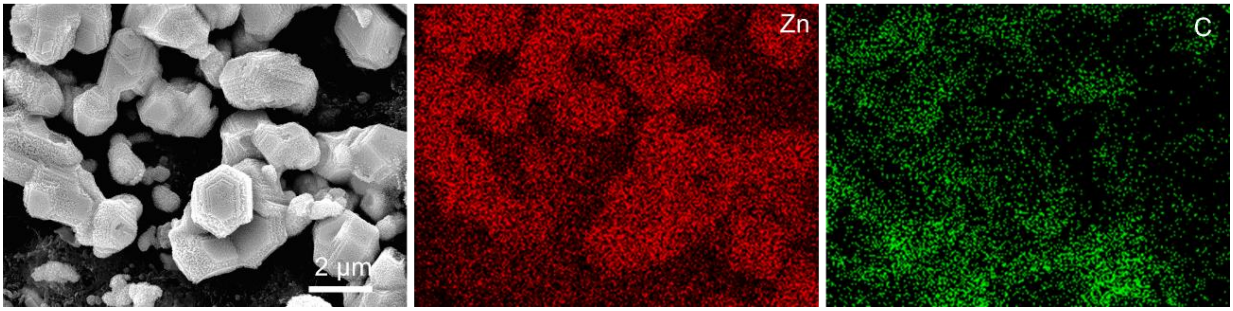

Fig. S23. SEM image corresponding EDS mapping of ZZG composite anode at discharge/reduction state.

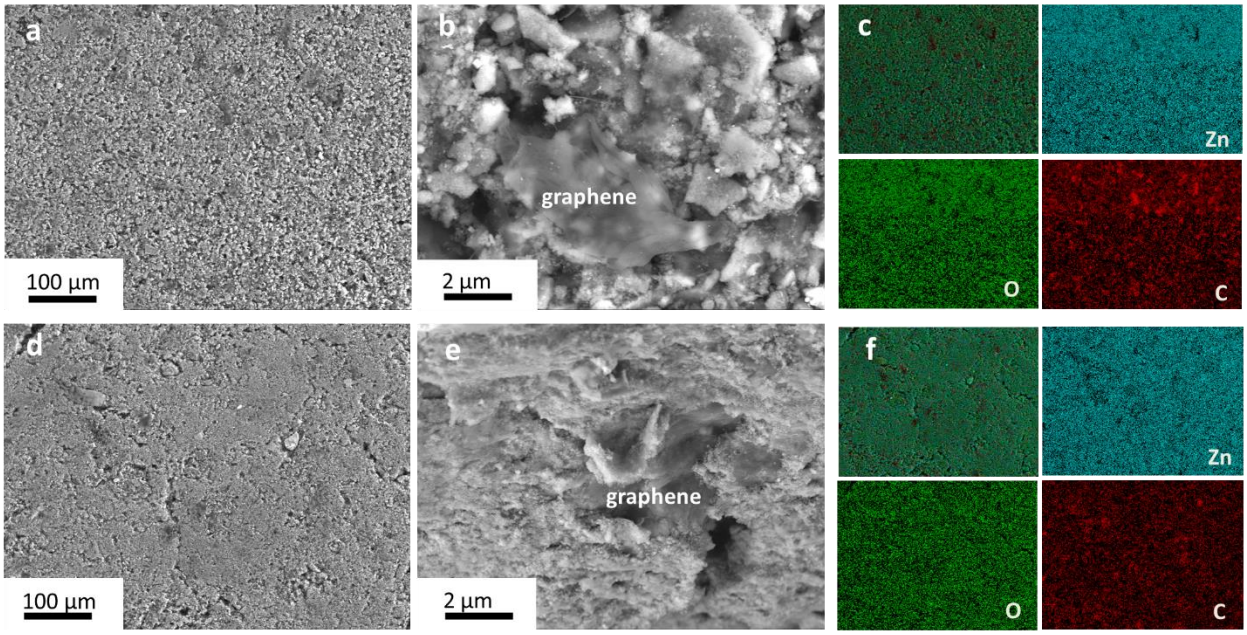

Fig. S24. SEM and EDS mapping images of ZZG before and after 100 cycles. (a) and (b) SEM images of ZZG before cycling at different grade. (c) Corresponding EDS mapping images of ZZG before cycling. (d) and (e) SEM images of ZZG anode after 100 cycles. (f) Corresponding EDS mapping images of ZZG anode after 100 cycles.

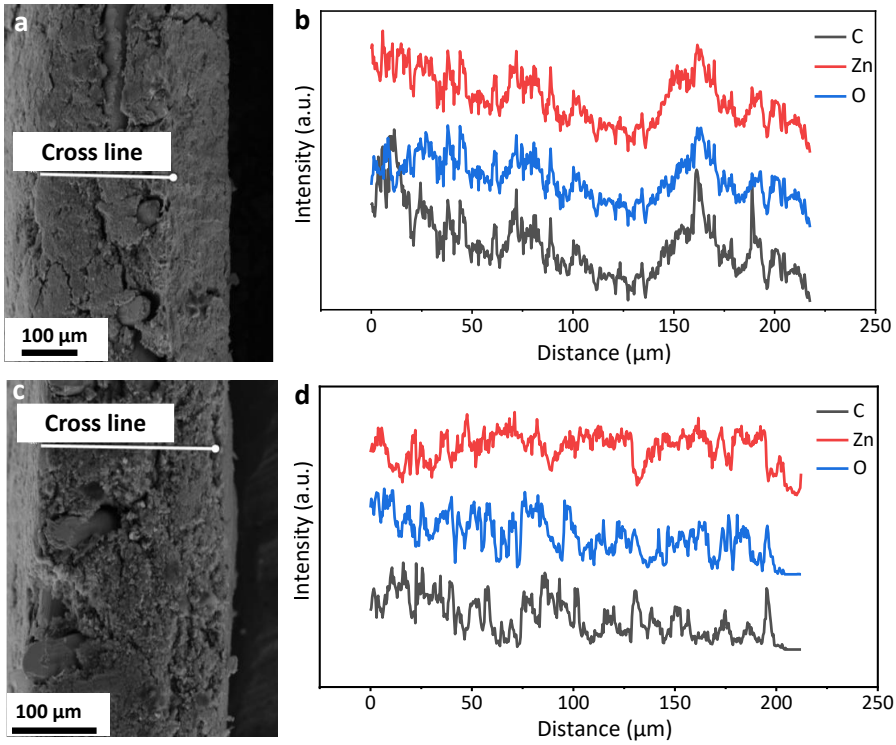

Fig. S25. SEM and EDS line scan of ZZG electrode before and after cycling. (a) The cross-sectional SEM image of ZZG electrode before cycling and (b) the corresponding EDS line scan of Zn, C and O elements. (c) and (d) The cross-sectional SEM image of ZZG electrode after 100 cycles and the corresponding EDS line scan of Zn, C and O elements.

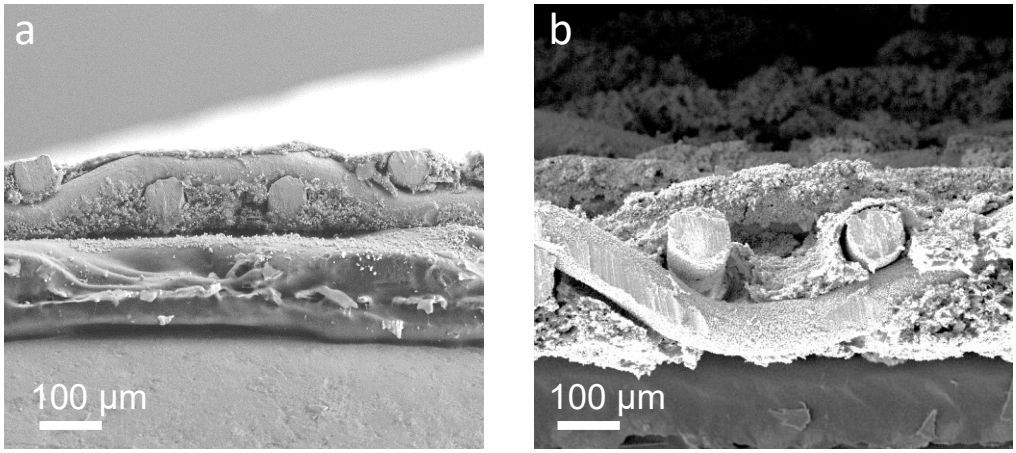

Fig. S26. The cross-sectional SEM images after cycles. (a) ZZG electrode after 3500 cycles in 2 M K_2CO_3 electrolyte. (b) Zn electrode after 50 cycles in 6 M KOH with saturated ZnO electrolyte.

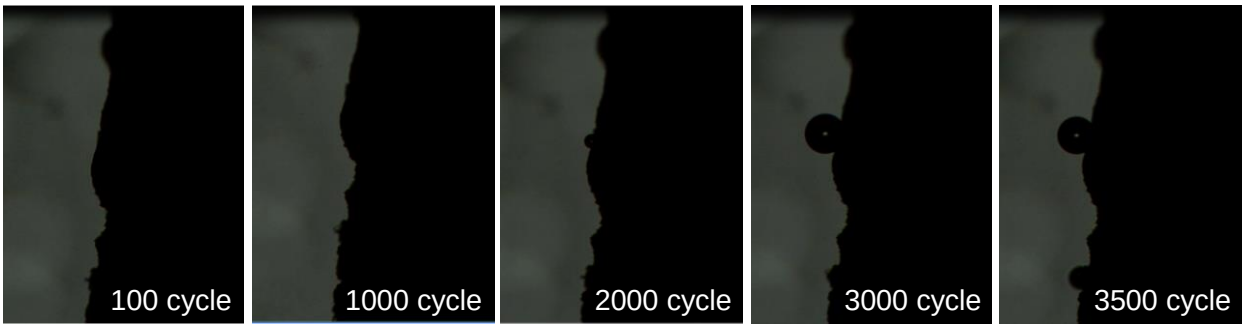

Fig. S27. *In-situ* optical microscope images of ZZG electrodes at different cycles. It is tested in a homemade transparent cell at cycles from 100 to 3500.

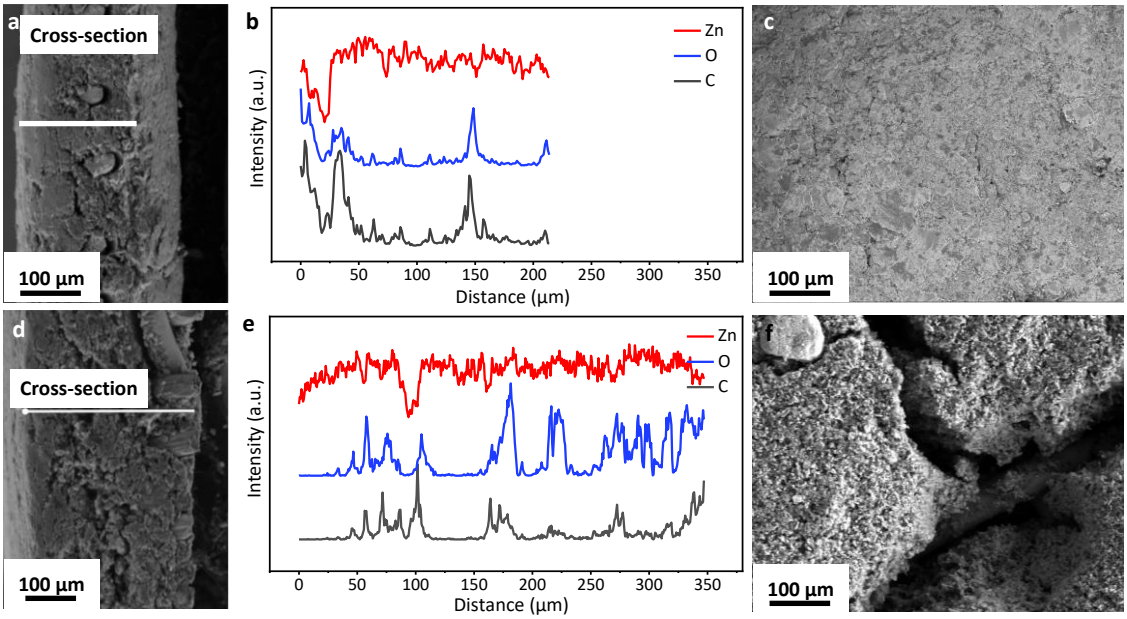

Fig. S28. SEM images and EDS line scan of $2ZnCO_3 \cdot 3Zn(OH)_2$ nanoparticle electrode before and after cycling. (a) The cross-sectional SEM image of $2ZnCO_3 \cdot 3Zn(OH)_2$ nano particle electrode before cycling and (b) the corresponding EDS line scan of Zn, C and O elements. (c) The SEM image before cycling from front view. (d) and (e) The cross-sectional SEM image of $2ZnCO_3 \cdot 3Zn(OH)_2$ nano particle electrode after 100 cycles and the corresponding EDS line scan of Zn, C and O elements. (f) The SEM image after 100 cycles from front view.

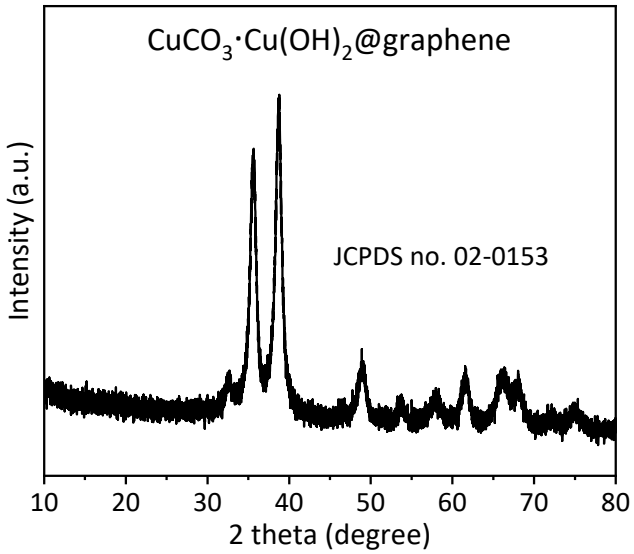

Fig. S29. XRD pattern of as-prepared $CuCO_3 \cdot Cu(OH)_2$@graphene composite.

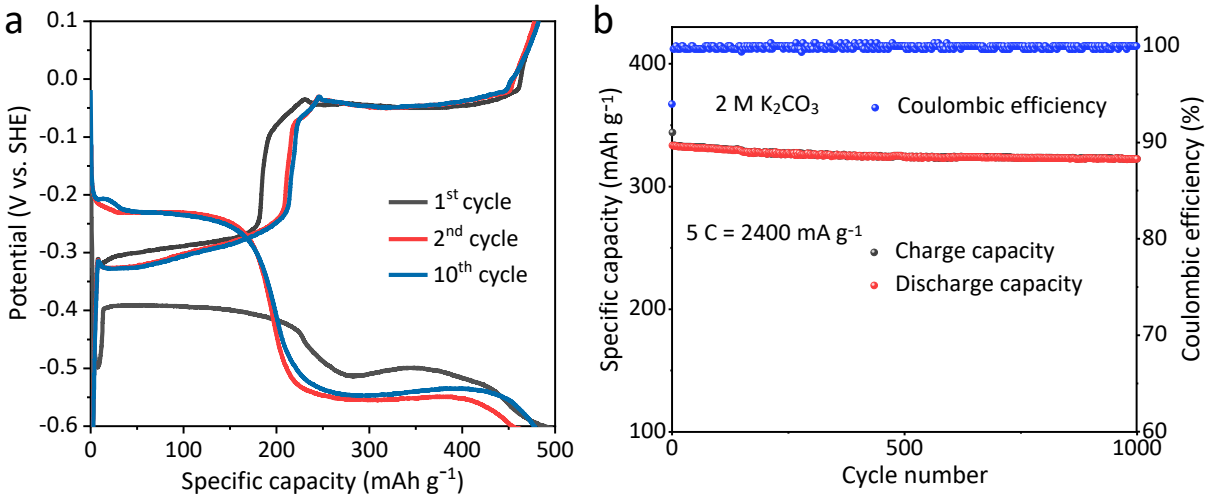

Fig. S30. Electrochemical performances of $CuCO_3 \cdot Cu(OH)_2$@graphene anode. (a) Galvanostatic discharge/charge curves of $CuCO_3 \cdot Cu(OH)_2$@graphene anode in 2 M K_2CO_3 electrolyte at 0.5 C within 0.1 V and −0.6 V vs. SHE. (b) Long cycle stability of $CuCO_3 \cdot Cu(OH)_2$@graphene anode in 2 M K_2CO_3 electrolyte at 5 C within 0.1 V and −0.6 V vs. SHE.

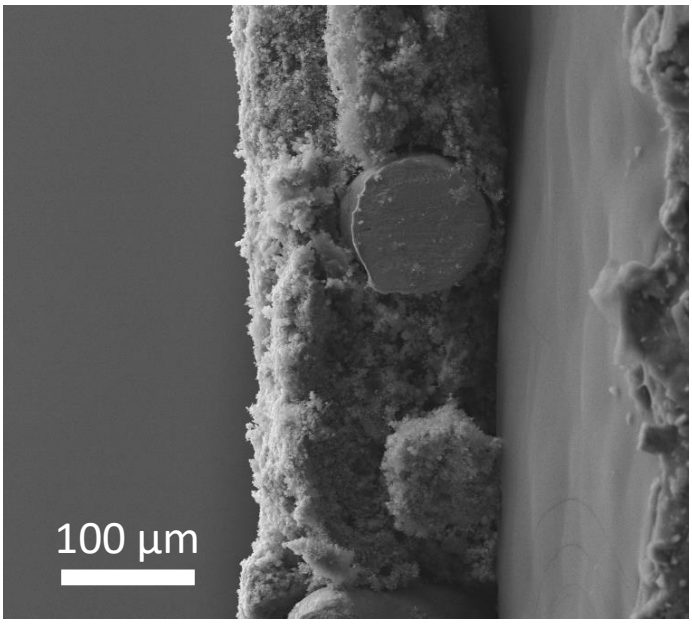

Fig. S31. SEM images of $CuCO_3 \cdot Cu(OH)_2$@graphene anode after 1000 cycles from a side view.

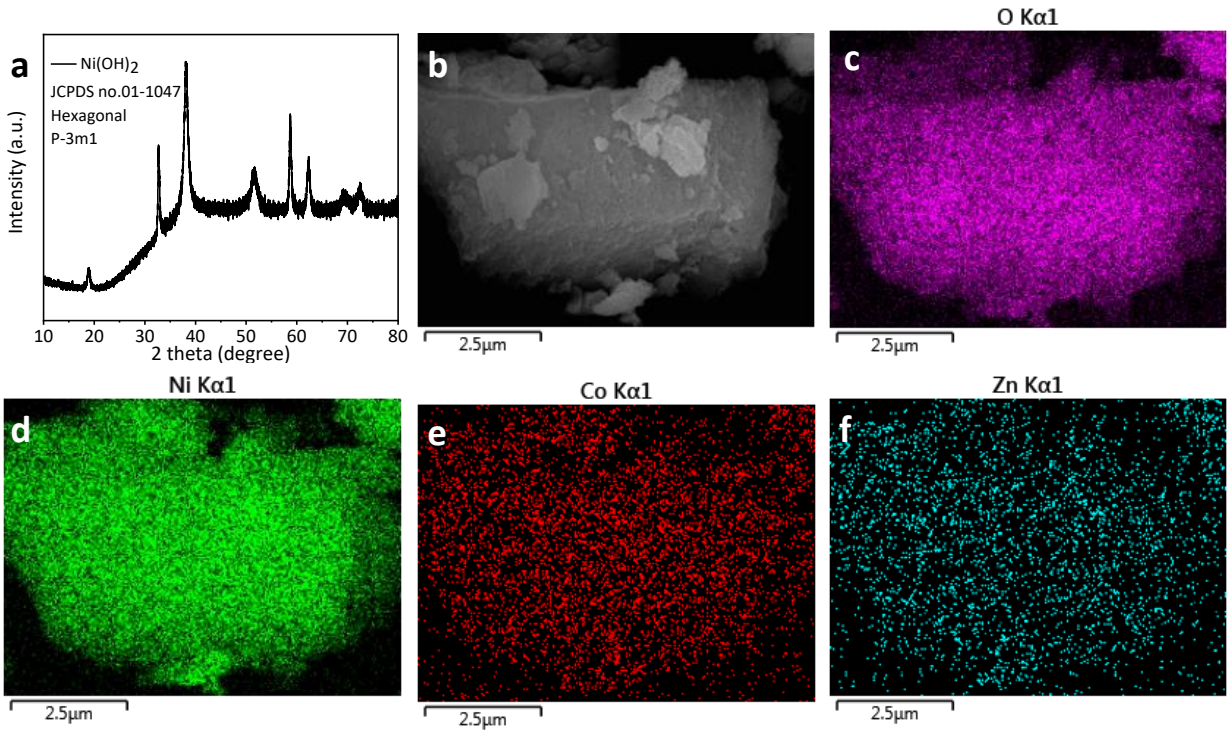

Fig. S32. Structure and morphology of cathode. (a) XRD pattern of as-prepared $Ni_{0.95}Co_{0.03}Zn_{0.02}(OH)_2$ sample. (b) SEM image of as-prepared $Ni_{0.95}Co_{0.03}Zn_{0.02}(OH)_2$ sample. (c), (d), (e) and (f) EDS mapping images of O, Ni, Co, and Zn elements, respectively.

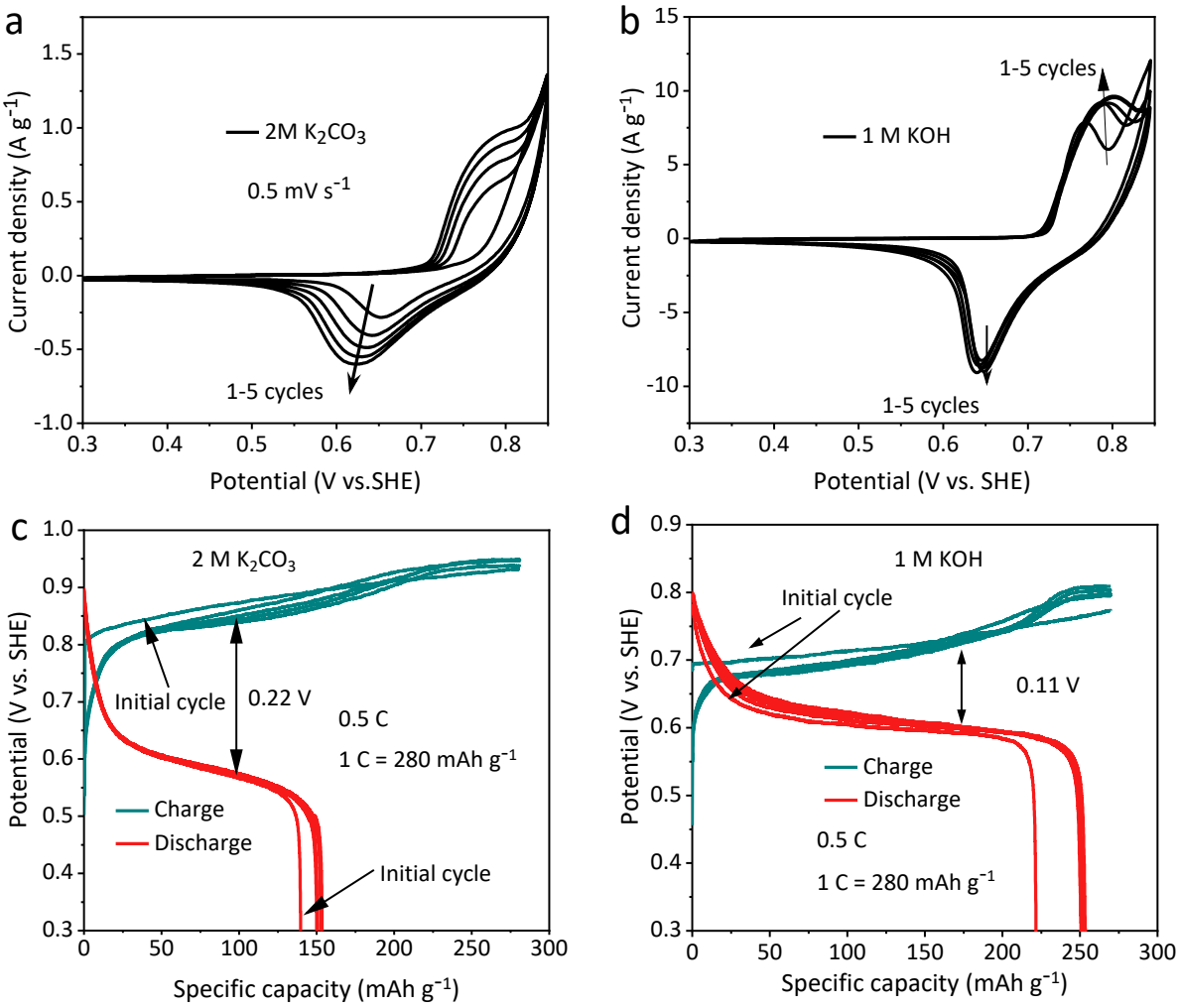

Fig. S33. Electrochemical characteristics of the cathode in different electrolytes. (a) CV results of $Ni_{0.95}Co_{0.03}Zn_{0.02}(OH)_2$ cathode in 2 M K_2CO_3 electrolyte at a scan rate of 0.5 mV s^{-1} between 0.3 and 0.85 V vs. SHE. (b) CV results of $Ni_{0.95}Co_{0.03}Zn_{0.02}(OH)_2$ cathode in 1 M KOH electrolyte at a scan rate of 0.5 mV s^{-1} between 0.3 and 0.85 V *vs.* SHE. (c) Charge and discharge curves of $Ni_{0.95}Co_{0.03}Zn_{0.02}(OH)_2$ cathode in 2 M K_2CO_3 electrolyte at a scan of 0.5 C. (d) Charge and discharge curves of $Ni_{0.95}Co_{0.03}Zn_{0.02}(OH)_2$ cathode in 1 M KOH electrolyte at a rate of 0.5 C. The cathode was fully charged at 0.5 C for two hours and then discharged at 0.5 C to 0.3 V *vs.* SHE.

Supplementary Note S5: **Discussion of $Ni_{0.95}Co_{0.03}Zn_{0.02}(OH)_2$ cathode.**

The peak current density is merely 0.5 A g^{-1} at a scan rate of 0.5 mV s^{-1} for the $Ni_{0.95}Co_{0.03}Zn_{0.02}(OH)_2$ cathode in 2 M K_2CO_3 electrolyte, which is much smaller than that in 1 M KOH electrolyte (Supplementary Fig. 33a and b). The voltage hysteresis between charge and discharge platform in Supplementary Fig. 33c and d is *ca*. 0.22 V, which is much higher than that in 1 M KOH electrolyte (*ca.* 0.11 V) at 0.5 C rate (1C is defined as 280 mA g^{-1}). Moreover, the discharge capacity of this cathode in 2 M K_2CO_3 is only 150 mAh g^{-1}, which is much smaller than that of 1 M KOH electrolyte (250 mAh g^{-1}).

According to the released capacity of 248 mAh g^{-1}, the practical reaction process of $Ni_{0.95}Co_{0.3}Zn_{0.2}(OH)_2$ cathode in our practical full cell should be:

$$Ni_{0.95}Co_{0.3}Zn_{0.2}(OH)_2 \leftrightarrow Ni_{0.95}Co_{0.3}Zn_{0.2}O_{0.86}OH_{1.14} + 0.86\ H^+ + 0.86\ e^-$$

Taking the charge balance into consideration, the practical reaction process at $2ZnCO_3{\cdot}3Zn(OH)_2$ anode would be:

$$0.086\ (2ZnCO_3{\cdot}3Zn(OH)_2) + 0.86\ e^- \leftrightarrow 0.43\ Zn + 0.172\ CO_3^{2-} + 0.516\ OH^-$$

The possible practical reaction processes of full cell can then be preliminarily formulated as:

$$Ni_{0.95}Co_{0.3}Zn_{0.2}(OH)_2 + 0.086\ (2ZnCO_3{\cdot}3Zn(OH)_2) + 0.172\ CO_3^{2-} \leftrightarrow$$
$$0.43\ Zn + 0.344\ HCO_3^- + Ni_{0.95}Co_{0.3}Zn_{0.2}O_{0.86}OH_{1.14} + 0.516\ H_2O$$

It should be noted that the electrolyte can provide enough CO_3^{2-} and OH^- to balance the H_2CO_3 intermediate and avoid CO_2 release. After 100 cycles in the full cell, the pH of the electrolyte is about 11 at a fully charged state. Whilst the pH of 2 M K_2CO_3 + 0.1 M KOH with saturated CO_2 is measured at about 8. Therefore, the pH of the electrolyte in the full cell keeps as weak alkaline before and after cycles (a pH value of 12.85 for the original electrolyte of 2 M K_2CO_3 + 0.1 M KOH), suggesting the absence of CO_2 gas in another way. These electrochemical process analyses and experimental verification guarantees the practicality of the batteries.

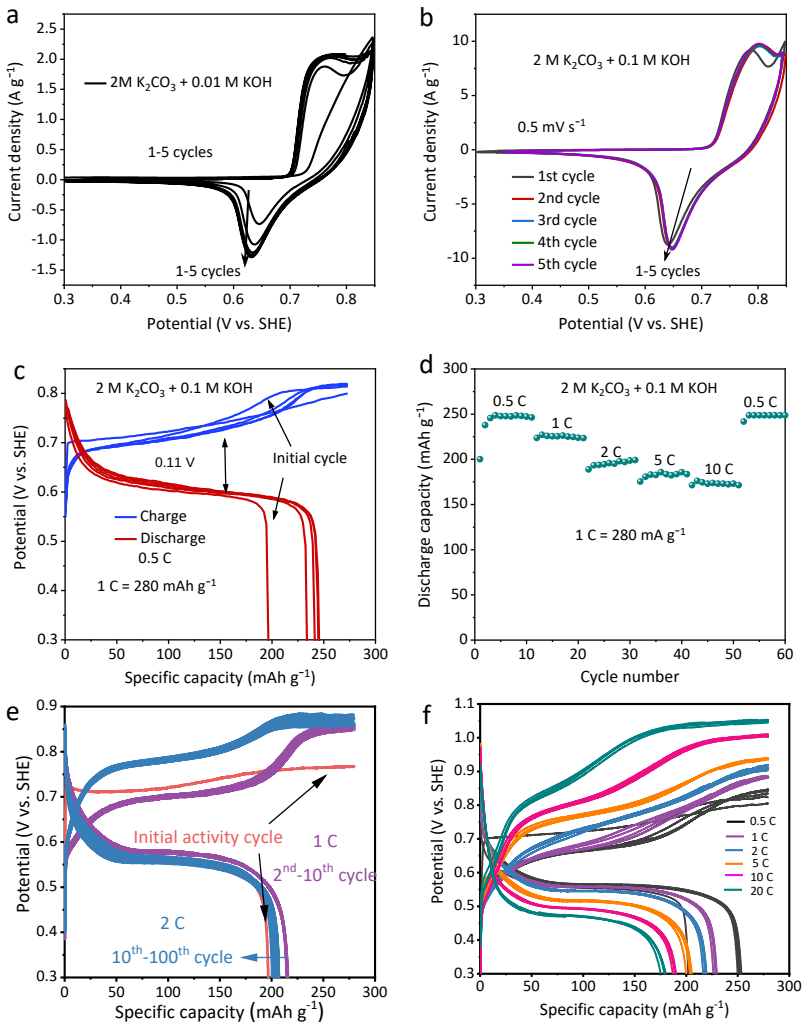

Fig. S34. Electrochemical characteristics of the cathode in 2 M K_2CO_3 +0.01 M KOH and 2 M K_2CO_3 +0.1 M KOH electrolytes. (a) CV results of $Ni_{0.95}Co_{0.03}Zn_{0.02}(OH)_2$ cathode in 2 M K_2CO_3 +0.01 M KOH electrolyte at a scan rate of 0.5 mV s^{-1} between 0.3 and 0.85 V vs. SHE. (b) CV results of $Ni_{0.95}Co_{0.03}Zn_{0.02}(OH)_2$ cathode in 2 M K_2CO_3 +0.1 M KOH electrolyte at a scan rate of 0.5 mV s^{-1} between 0.3 and 0.85 V *vs.* SHE. (c) Charge and discharge curves of $Ni_{0.95}Co_{0.03}Zn_{0.02}(OH)_2$ cathode in 2 M K_2CO_3 +0.1 M KOH electrolyte at a rate of 0.5 C. The cathode was fully charged at 0.5 C for two hours and then discharged at 0.5 C to 0.3 V vs. SHE. (d) Rate capability of $Ni_{0.95}Co_{0.03}Zn_{0.02}(OH)_2$ cathode in 2 M K_2CO_3 +0.1 M KOH electrolyte. The cathode was fully charged at 0.5 C for two hours and then discharged at different rates to 0.3 V *vs.* SHE. (e) Charge and discharge curves and (f) rate-capability of $Ni_{0.95}Co_{0.03}Zn_{0.02}(OH)_2$ cathode in 2 M K_2CO_3 electrolyte after fully activating in 2 M K_2CO_3 + 0.1 M KOH electrolyte, which is fully charged at 0.5 C for two hours and then discharged at 0.5 C to 0.3 V *vs.* SHE.

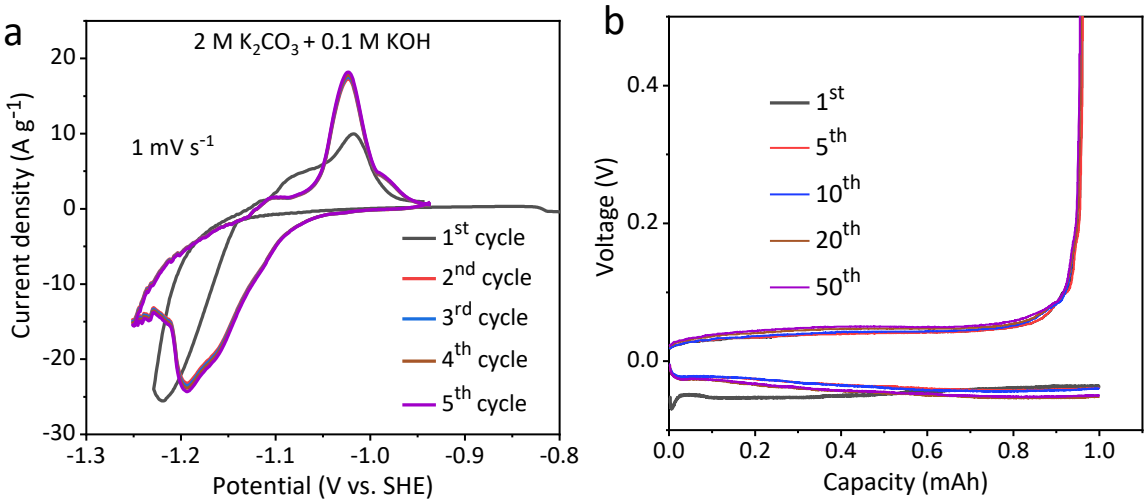

Fig. S35. Electrochemical performances of ZZG in 2 M K_2CO_3 + 0.1 M KOH electrolyte. (a) CV results of ZZG anode in 2 M K_2CO_3 + 0.1 M KOH electrolyte at a scan rate of 1 mV s^{-1} vs. SHE. (b) Charge-discharge voltage gap of ZZG || Zn asymmetric cells in 2 M K_2CO_3+0.1M KOH electrolyte at different cycles with current density of 1 mA cm^{-2} and capacity of 1 mAh cm^{-2}.

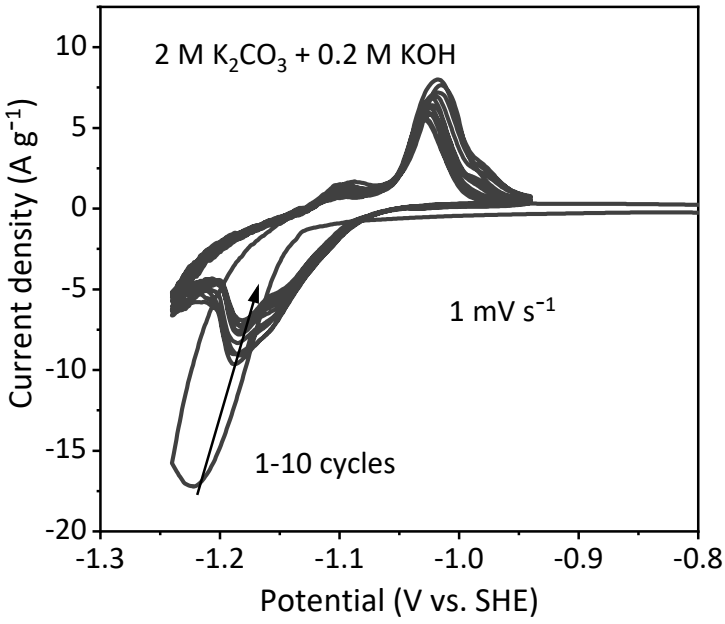

Fig. S36. CV results of ZZG anode in 2 M K_2CO_3 +0.2 M KOH electrolyte. The scan rate is 1 mV s^{-1} *vs.* SHE.

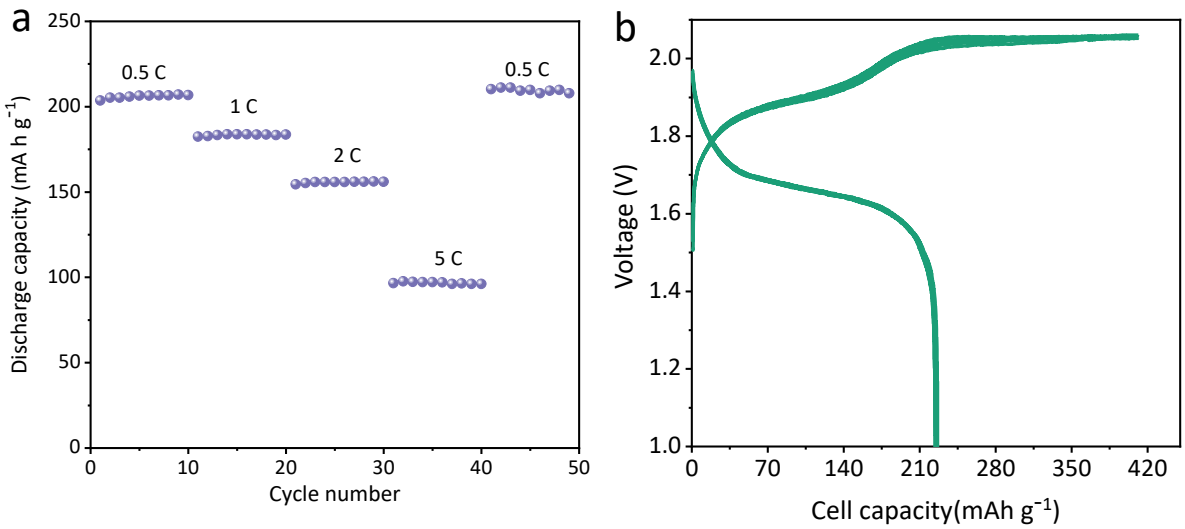

Fig. S37. Low temperature and overcharge performances of full cell. (a) Rate-capability of Ni-ZZG full cell at a low temperature of −20 ºC. (b) Overcharge tests of Ni-ZZG full cell.

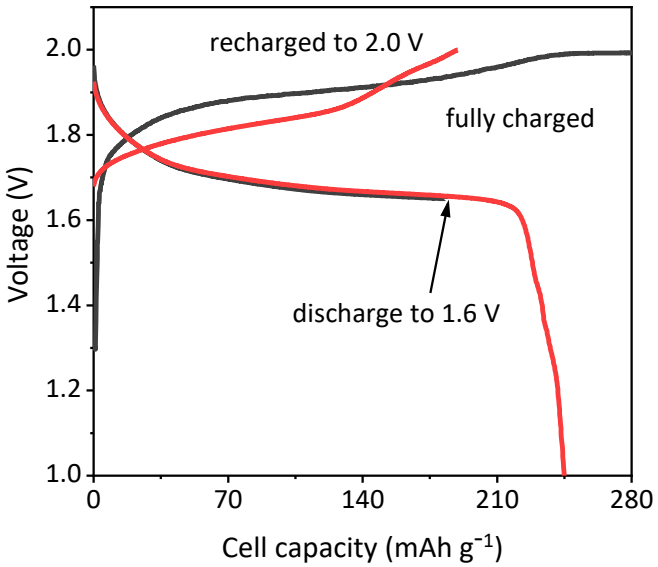

Fig. S38. Memory effect tests of Ni-ZZG full cell. The battery was firstly fully charged to 2.0 V and discharged to 1.6 V. Then the battery was recharged to 2.0 V. After that, the battery was discharged to 1.0 V.

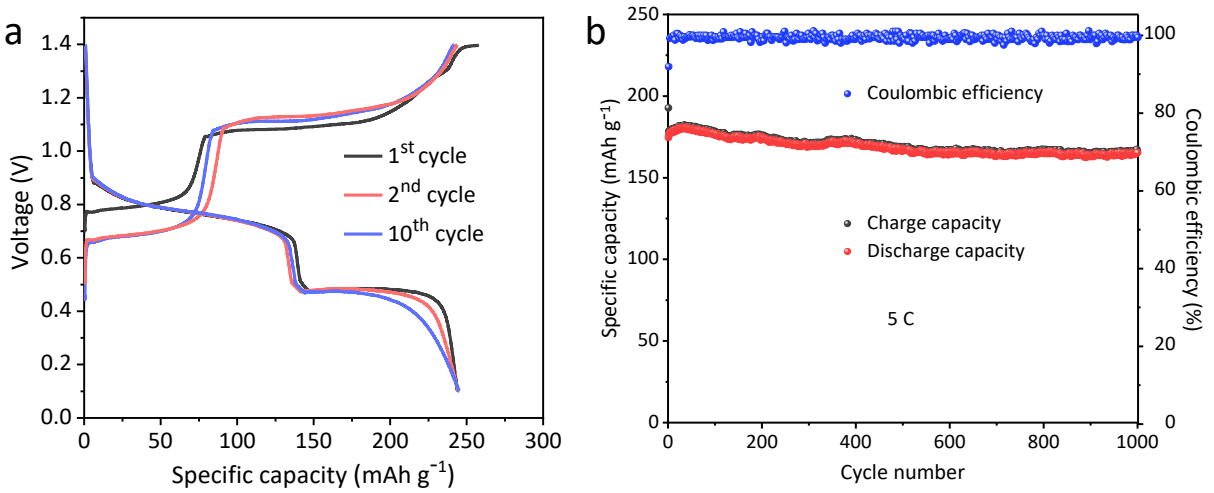

Fig. S39. Electrochemical performances of $Ni_{0.95}Co_{0.3}Zn_{0.2}(OH)_2$-$CuCO_3 \cdot Cu(OH)_2$@graphene battery. (a) The typical charge/discharge profiles of the $Ni_{0.95}Co_{0.3}Zn_{0.2}(OH)_2$-$CuCO_3 \cdot Cu(OH)_2$@graphene battery in 2 M K_2CO_3 + 0.1 M KOH electrolyte between 0.1 V and 1.4 V at 0.5 C. (b) Long cycle stability of $Ni_{0.95}Co_{0.3}Zn_{0.2}(OH)_2$-$CuCO_3 \cdot Cu(OH)_2$@graphene battery in 2 M K_2CO_3 +0.1 M KOH electrolyte at 5 C within 0.1 V and 1.4 V.

Table S1. The calculation of CO_3^{2-} transference number.

E (V)	Io (mA)	Iss(mA)	Ro(Ω)	Rss(Ω)	tCO_3^{2-}
0.01	0.084	0.033	4.0	15.1	0.4

Table S2. Zinc utilization of various Zn-batteries reported in recent years.

Cathode//anode materials	Electrolyte	Zinc utilization	Cycling stability	Ref.
$LiMn_2O_4$ || Zn	1 m $Zn(TFSI)_2$ + 20 m LiTFSI	17%	4000(80%)	3
$VOPO_4$ || Zn	4 m $Zn(OTF)_2$ + 0.5 m $Me_3EtNOTF$	33%	6000(88.7%)	17
Zn-air		68%	300	
NiOOH || Zn	6 M KOH + 1 M LiOH + 11 wt% $Ca(OH)_2$	40%	100	23
$Zn_2(OH)VO_4$ || Zn	gel electrolyte	66%	2000(89%)	24
α-MnO_2 || Zn	2M $ZnSO_4$	50%	1000(65%)	25
$Ni(OH)_2$ || ZnO	4M KOH + 2M KF + 1M K_2CO_3 + saturated ZnO	50%	400(89.4%)	35
I_2 || Zn	1 M KI + 0.2 M $ZnSO_4$	34%	300(100%)	37
$2ZnCO_3 \cdot 3Zn(OH)_2$ || Ni-based full cell	2M K_2CO_3 + 0.1M KOH	91.3%	2000(80%)	**This work**

Table S3. Comparison of the electrochemical performances in different types of aqueous batteries.

Cathode//anode materials	Electrolyte	Voltage /V	Energy density (power density) /Wh kg^{-1} (W kg^{-1})	Cycles (retention) /cycle No.(%)	Ref.
$Li_2Mn_2O_4$ || Zn	1 m $Zn(TFSI)_2$ + 20 m LiTFSI	1.8	180(43)	4000(80%)	3
$VOPO_4$ || Zn	4 m $Zn(OTF)_2$ + 0.5 m $Me_3EtNOTF$	0.8	100(95)	6000(88.7%)	17
$Zn_2(OH)VO_4$ || Zn	gel electrolyte	0.9	140(70)	2000(89%)	24
$Zn_{0.25}V_2O_5 \cdot nH_2O$ || Zn	1M $ZnSO_4$	0.81	150(60)	1000(80%)	2
β-MnO_2 || Zn	3M $Zn(CF_3SO_3)_2$ + 0.1M $MnSO_4$	1.3	254(197)	2000(94%)	38
$LiMn_2O_4$ || Mo_6S_8	21 m LiTFSI	2.0	100(50)	1000(68%)	39
$LiNi_{0.5}Mn_{1.5}O_4$ || $Li_4Ti_5O_{12}$	21 m LiTFSI + 9mDEC	3.2	165(80)	1000(70%)	40
$LiCoO_2$ || Mo_6S_8	21 m LiTFSI-0.1 wt% TMSB	2.0	80(150)	100(92%)	41
$LiCoO_2$ || $Li_4Ti_5O_{12}$	$Li(TFSI)_{0.7}(BETI)_{0.3} \cdot 2H_2O$ hydrate-melt	2.4	130(150)	200(60%)	42
$2ZnCO_3 \cdot 3Zn(OH)_2$ || Ni-based full cell	2M K_2CO_3 + 0.1M KOH	1.69	270(152)	2000(80%)	**This work**

Supplementary Note S6:

Energy and power calculations.

The specific energy of a full cell (E) is calculated as the product of the cell voltage (V_{cell}) and cell specific capacity (C_{cell})

$E = V_{cell} \times C_{cell}$

C_{cell} is typically calculated from the specific capacities of cathode and anode. In this work, the full cell capacity is calculated only based on the mass of the cathode. So, the C_{cell} should be:

C_{cell} = (full cell capacity)/(total mass of cathode and anode)

For example:

the energy density of as-prepared $Ni_{0.95}Co_{0.03}Zn_{0.02}(OH)_2$-ZZG full cell at 0.5 C:

$E = 1.69\ V \times 248\ Ah/(1+1/1.8)\ kg = 270\ Wh\ kg^{-1}$

at 10 C rate:

$E = 1.5\ V \times 170\ Ah/(1+1/1.8)\ kg = 164\ Wh\ kg^{-1}$

Considering the mass of the electrolyte, the C_{cell} should be:

C_{cell} = (full cell capacity)/(total mass of cathode, anode and electrolyte)

For example:

the energy density of as-prepared $Ni_{0.95}Co_{0.03}Zn_{0.02}(OH)_2$-ZZG full cell using 2 M K_2CO_3 + 0. 1 M KOH weak alkaline electrolyte at 0.5 C (the density of electrolyte is about 1.1 g cm^{-3}):

$E = 1.69\ V \times 248\ Ah/(1+1/1.8+1.1)\ kg = 160\ Wh\ kg^{-1}$

The specific power energy of a full cell (P) is calculated as the product of the cell voltage (V_{cell}) and specific discharge current (I_{cell})

$P = V_{cell} \times I_{cell}$

For example:

the power density of as-prepared $Ni_{0.95}Co_{0.03}Zn_{0.02}(OH)_2$-ZZG full cell using 2 M K_2CO_3 + 0. 1 M KOH weak alkaline electrolyte at 0.5 C rate:

$P = 1.69\ V \times 140\ A/(1+1/1.8) = 152\ W\ kg^{-1}$

at 10 C rate:

$P = 1.5\ V \times 2800\ A/(1+1/1.8) = 2709\ W\ kg^{-1}$

REFERENCES AND NOTES

1. H. Pan, Y. Shao, P. Yan, K. S. Han, Z. Nie, C. Wang, J. Yang, X. Li, P. Bhattacharya, K. T. Mueller, J. Liu, Reversible aqueous zinc/manganese oxide energy storage from conversion reactions. *Nat. Energy* **1**, 1–7 (2016).

2. D. Kundu, B. D. Adams, V. Duffort, S. H. Vajargah, L. F. Nazar, A high-capacity and long-life aqueous rechargeable zinc battery using a metal oxide intercalation cathode. *Nat. Energy* **1**, 1–8 (2016).

3. F. Wang, O. Borodin, T. Gao, X. Fan, W. Sun, F. Han, A. Faraone, J. A. Dura, K. Xu, C. Wang, Highly reversible zinc metal anode for aqueous batteries. *Nat. Mater.* **17**, 543–549 (2018).

4. M. Song, H. Tan, D. Chao, H. J. Fan, Recent advances in Zn-ion batteries. *Adv. Funct. Mater.* **28**, 1802564 (2018).

5. D. Chao, W. Zhou, F. Xie, C. Ye, H. Li, M. Jaroniec, S.-Z. Qiao, Roadmap for advanced aqueous batteries: From design of materials to applications. *Sci. Adv.* **6**, eaba4098 (2020).

6 C. Xu, B. Li, H. Du, F. Kang, Energetic zinc ion chemistry: The rechargeable zinc ion battery. *Angew. Chem. Int. Ed.* **51**, 933–935 (2012).

7. M. Matsushita, M. Sano, Y. Hayakawa, H. Honjo, Y. Sawada, Fractal structures of zinc metal leaves grown by electrodeposition. *Phys. Rev. Lett.* **53**, 286–289 (1984).

8. D. Grier, E. Ben-Jacob, R. Clarke, L.-M. Sander, Morphology and microstructure in electrochemical deposition of zinc. *Phys. Rev. Lett.* **56**, 1264–1267 (1986).

9. F. R. McLarnon, E. J. Cairns, The secondary alkaline zinc electrode. *J. Electrochem. Soc.* **138**, 645–656 (1991).

10. K. Bass, P. Mitchell, G. Wilcox, J. Smith, Methods for the reduction of shape change and dendritic growth in zinc-based secondary cells. *J. Power Sources* **35**, 333–351 (1991).

11. T. B. Reddy, *Linden's Handbook of Batteries* (McGraw-Hill, 2011), vol. 4.

12. J. Hao, J. Long, B. Li, X. Li, S. Zhang, F. Hua, X. Zeng, Z. Yang, W. Pang, Z. Guo, Toward high-performance hybrid zn-based batteries via deeply understanding their mechanism and using electrolyte additive. *Adv. Funct. Mater.* **29**, 1903605 (2019).

13. Q. Zhang, J. Luan, L. Fu, S. Wu, Y. Tang, X. Ji, H. Wang, The three-dimensional dendrite-free zinc anode on a copper mesh with a zinc-oriented polyacrylamide electrolyte additive. *Angew. Chem. Int. Ed.* **58**, 15841–15847 (2019).

14. P. Sun, L. Ma, W. Zhou, M. Qiu, Z. Wang, D. Chao, W. Mai, Simultaneous regulation on solvation shell and electrode interface for dendrite-free Zn ion batteries achieved by a low-cost glucose additive. *Angew. Chem.* **133**, 18395–18403 (2021).

15. Z. Yuan, X. Liu, W. Xu, Y. Duan, H. Zhang, X. Li, Negatively charged nanoporous membrane for a dendrite-free alkaline zinc-based flow battery with long cycle life. *Nat. Commun.* **9**, 1–11 (2018).

16. J. Zheng, J. Yin, D. Zhang, G. Li, D. C. Block, T. Tang, Q. Zhao, X. Liu, A. Warren, Y. Deng, S. Jin, A. C. Marschilok, E. S. Takeuchi, K. J. Takeuchi, C. D. Rahn, L. A. Archer, Spontaneous and field-induced crystallographic reorientation of metal electrodeposits at battery anodes. *Sci. Adv.* **6**, eabb1122 (2020).

17. L. Cao, D. Li, T. Pollad, T. Deng, B. Zhang, C. Yang, L. Chen, J. Vatamanu, E. Hu, M. J. Hourwitz, L. Ma, M. Ding, Q. Li, S. Hou, K. Gaskell, G. T. Fourkas, X.-Q. Yang, K. Xu, O. Borodin, C. Wang, Fluorinated interphase enables reversible aqueous zinc battery chemistries. *Nat. Nanotech.* **16**, 902–910 (2021).

18. J. Hao, X. Li, S. Zhang, F. Yang, X. Zeng, S. Zhang, G. Bo, C. Wang, Z. Guo, Designing dendrite-free zinc anodes for advanced aqueous zinc batteries. *Adv. Funct. Mater.* **30**, 2001263 (2020).

19. Z. Wang, J. Hu, L. Han, Z. Wang, H. Wang, Q. Zhao, J. Liu, F. Pan, A MOF-based single-ion Zn^{2+} solid electrolyte leading to dendrite-free rechargeable Zn batteries. *Nano Energy* **56**, 92–99 (2019).

20. X. Xie, S. Liang, J. Gao, S. Guo, J. Guo, C. Wang, G. Xu, X. Wu, G. Chen, J. Zhou, Manipulating the ion-transfer kinetics and interface stability for high-performance zinc metal anodes. *Energ. Environ. Sci.* **13**, 503–510 (2020).

21. L. Cao, D. Li, T. Deng, Q. Li, C. Wang, Hydrophobic organic-electrolyte-protected zinc anodes for aqueous zinc batteries. *Angew. Chem. Int. Ed.* **59**, 19292–19296 (2020).

22. Y. Cui, Q. Zhao, X. Wu, X. Chen, J. Yang, Y. Wang, R. Qin, S. Ding, Y. Song, J. Wu, K. Yang, Z. Wang, Z. Mei, Z. Song, H. Wu, Z. Jiang, G. Qian, L. Yang, F. Pan, An interface-bridged organic–inorganic layer that suppresses dendrite formation and side reactions for ultra-long-life aqueous zinc metal anodes. *Angew. Chem. Int. Ed.* **59**, 16594–16601 (2020).

23. J. F. Parker, C. N. Chervin, I. R. Pala, M. Machler, M. F. Burz, J. W. Long, D. R. Rolison, Rechargeable nickel–3D zinc batteries: An energy-dense, safer alternative to lithium-ion. *Science* **356**, 415–418 (2017).

24. D. Chao, C. Zhu, M. Song, P. Liang, X. Zhang, N. H. Tiep, H. Zhao, J. Wang, R. Wang, H. Zhang, H. J. Fan, A high-rate and stable quasi-solid-state zinc-ion battery with novel 2D layered zinc orthovanadate array. *Adv. Mater.* **30**, e1803181 (2018).

25 J. Zheng, Q. Zhao, T. Tang, J. Yin, C. D. Quilty, G. D. Renderos, X. Liu, Y. Deng, L. Wang, D. C. Bock, C. Jaye, D. Zhang, E. S. Takeuchi, K. J. Takeuchi, A. C. Marschilok, L. A. Archer, Reversible epitaxial electrodeposition of metals in battery anodes. *Science* **366**, 645–648 (2019).

26. P. P. Lopes, V. R. Stamenkovic, Past, present, and future of lead–acid batteries. *Science* **369**, 923–924 (2020).

27. H. Bode, *Lead-Acid Batteries* (John Wiley and Sons Inc., 1977).

28. Y. Hu, J. Yang, J. Hu, J. Wang, S. Liang, H. Hou, X. Wu, B. Liu, W. Yu, X. He, R. V. Kumar, Lead-carbon batteries: Synthesis of nanostructured PbO@C composite derived from spent lead-acid battery for next-generation lead-carbon battery (Adv. Funct. Mater. 9/2018). *Adv. Funct. Mater.* **28**, 1870056 (2018).

29. D. Pavlov, *Lead-Acid Batteries: Science and Technology*, D. Pavlov, Ed. (Elsevier, 2011), pp. 29–114.

30. W. M. Haynes, *CRC Handbook of Chemistry and Physics* (CRC Press, 2014).

31. J. G. Speight, *Lange's Handbook of Chemistry* (McGraw-Hill Education, 2017).

32. Z. Chen, T. Yuan, X. Pu, H. Yang, X. Ai, Y. Xia, Y. Cao, Symmetric sodium-ion capacitor based on $Na_{0.44}MnO_2$ nanorods for low-cost and high-performance energy storage. *ACS Appl. Mater. Inter.* **10**, 11689–11698 (2018).

33. J. Liu, M. Chen, L. Zhang, J. Jiang, J. Yan, Y. Huang, J. Lin, H. J. Fan, Z. X. Shen, A flexible alkaline rechargeable ni/fe battery based on graphene foam/carbon nanotubes hybrid film. *Nano Lett.* **14**, 7180–7187 (2014).

34. J. E. Randles, A cathode ray polarograph. Part II. The current-voltage curves. *Trans. Faraday Soc.* **44**, 327–338 (1948).

35. W. Zhou, D. Zhu, J. He, J. Li, H. Chen, Y. Chen, D. Chao, A scalable top-down strategy toward practical metrics of Ni–Zn aqueous batteries with total energy densities of 165 W h kg^{-1} and 506 W h L^{-1}. *Energ. Environ. Sci.* **13**, 4157–4167 (2020).

36. M. E. Uñates, M. E. Folquer, J. R. Vilche, A. J. Arvia, The influence of foreign cations on the electrochemical behavior of the nickel hydroxide electrode. *J. Electrochem. Soc.* **139**, 2697–2704 (1992).

37. G. Liang, J. Zhu, B. Yan, Q. Li, A. Chen, Z. Chen, X. Wang, B. Xiong, J. Fan, J. Xu, C. Zhi, Gradient fluorinated alloy to enable highly reversible Zn-metal anode chemistry. *Energ. Environ. Sci.* **15**, 1086–1096 (2022).

38. N. Zhang, F. Cheng, J. Liu, L. Wang, X. Long, X. Liu, F. Li, J. Chen, Rechargeable aqueous zinc-manganese dioxide batteries with high energy and power densities. *Nat. Commun.* **8**, 1–9 (2017).

39. L. Suo, O. Borodin, T. Gao, M. Olguin, J. Ho, X. Fan, C. Luo, C. Wang, K. Xu, "Water-in-salt" electrolyte enables high-voltage aqueous lithium-ion chemistries. *Science* **350**, 938–943 (2015).

40. F. Wang, O. Borodin, M. S. Ding, M. Gobet, J. Vatamanu, X. Fan, T. Gao, N. Eidson, Y. Liang, W. Sun, S. Greenbaum, K. Xu, C. Wang, Hybrid aqueous/non-aqueous electrolyte for safe and high-energy li-ion batteries. *Joule* **2**, 927–937 (2018).

41. F. Wang, Y. Lin, L. Suo, X. Fan, T. Gao, C. Yang, F. Han, Y. Qi, X. Kang, C. Wang, Stabilizing high voltage $LiCoO_2$ cathode in aqueous electrolyte with interphase-forming additive. *Energ. Environ. Sci.* **9**, 3666–3673 (2016).

42. Y. Yamada, K. Usui, K. Sodeyama, S. Ko, Y. Tateyama, A. Yamada, Hydrate-melt electrolytes for high-energy-density aqueous batteries. *Nat. Energy* **1**, 1–9 (2016).

43. M. J. Abraham, T. Murtola, R. Schulz, S. Páll, J. C. Smith, B. Hess, E. Lindahl, GROMACS: High performance molecular simulations through multi-level parallelism from laptops to supercomputers. *SoftwareX* **1-2**, 19–25 (2015).

44. S. Pronk, S. Páll, R. Schulz, P. Larsson, P. Bjelkmar, R. Apostolov, M. R. Shirts, J. C. Smith, P. M. Kasson, D. Van Der Spoel, B. Hess, E. Lindahl, GROMACS 4.5: A high-throughput and highly parallel open source molecular simulation toolkit *Bioinformatics* **29**, 845–854 (2013).

45. G. Kresse, J. Furthmuller, Efficient iterative schemes for *ab initio* total-energy calculations using a plane-wave basis set. *Phys. Rev. B* **54**, 11169–11186 (1996).

46. J. P. Perdew, K. Burke, M. Ernzerhof, Generalized gradient approximation made simple. *Phys. Rev. Lett.* **77**, 3865–3868 (1996).